nature chemistry

SUPPLEMENTARY INFORMATION

https://doi.org/10.1038/s41557-018-0022-y

In the format provided by the authors and unedited.

Cooperative communication within and between single nanocatalysts

Ningmu Zou[1,5], Xiaochun Zhou[1,2,5], Guanqun Chen[1,5], Nesha May Andoy[1,3], Won Jung[1], Guokun Liu[1,4] and Peng Chen[1*]

[1]Department of Chemistry and Chemical Biology, Cornell University, Ithaca, NY, USA. [2]Present address: Suzhou Institute of Nano-Tech and Nano-Bionics, Chinese Academy of Sciences, Suzhou, Jiangsu, PR China. [3]Present address: BioMed X Innovation Center, Heidelberg, Germany. [4]Present address: College of the Environment and Ecology, Xiamen University, Xiamen, PR China. [5]These authors contributed equally: Ningmu Zou, Xiaochun Zhou and Guanqun Chen. *e-mail: pc252@cornell.edu

Supplementary Information

to

Co-operative Communication within and between Single Nanocatalysts

Ningmu Zou,[†] Xiaochun Zhou,[†,‡] Guanqun Chen,[†] Nesha May Andoy,[§] Won Jung, Guokun Liu,[¶] Peng Chen[*]

Department of Chemistry and Chemical Biology, Cornell University, Ithaca, NY 14853, U.S.A.

[†] Equal contribution. [‡] Present address: Suzhou Institute of Nano-Tech and Nano-Bionics, Chinese Academy of Sciences, 398 Ruoshui Road, Suzhou Industrial Park, Suzhou, Jiangsu 215123, P. R. China. [§] Present address: BioMed X Innovation Center, Im Neuenheimer Feld 515, 69120 Heidelberg, Germany. [¶] Present address: College of the Environment and Ecology, Xiamen University, Xiamen 361005, P.R. China. [*] Correspondence to: pc252@cornell.edu

Table of Content

1. Synthesis and characterization of nanocatalysts 3

2. Fluorogenic catalytic reactions, and ensemble assay shows that Pd nanorods can catalyze resazurin disproportionation to generate resorufin 5

3. Experimental setup for single-molecule fluorescence imaging, solution flow and voltage manipulations, as well as acetate and nitrite effects 6

4. Data processing for single-molecule fluorescence imaging, localization precision, and spatial resolution 7

5. The product resorufin stays on the nanorod for ~38 ms on average, orders of magnitude shorter than its photoblinking/bleaching on-time, and it stays essentially stationary within our localization precision before desorbing into solution 10

6. Analysis procedures of the *intra-* and *inter-particle* catalytic communications between temporally subsequent reactions that occur at different locations 11

6.1 Intraparticle catalytic communication within Pd or Au nanorods 11

6.2 Intraparticle catalytic communication within Au nanoplates 12

6.3 Interparticle catalytic communication between temporally subsequent reactions that occur on different particles 12

6.4 Spurious contributions to cross-correlation coefficients, reflected by the interparticle ρ_{τ_i,τ_j} at long distance and time separations, are used as a residual offset for the intraparticle ρ_{τ_i,τ_j} 13

6.5 Additional discussions on the reliability of the correlation analyses for demonstrating the intra- and inter-particle catalytic communication 13

7. Both intra- and inter-particle catalytic communication behaviors vanish if the temporal sequence, spatial locations, or both of the catalytic events on each nanocatalyst are randomized 14

8. Simulations show that temporally random catalytic events do not show intra- or inter-particle catalytic communications, but have a spurious residual cross correlation 17

9. Resorufin rebinding to nanocatalysts contributes to ~0.3% of the detected events and does *not* give rise to intra- or inter-particle catalytic communication behaviors 20

10. Additional experimental results 22

10.1 Additional results on Pd nanorods in catalyzing Rz disproportionation 22

10.2 Additional results on Au nanorods in catalyzing AR deacetylation 22

10.3 Results on Au nanorods in catalyzing Rz deoxygenation 23

10.4 Results on Au nanoplates in catalyzing Rz deoxygenation 25

10.5 The temporal memories t_0 of both intra- and inter-particle catalytic communications are unaffected by the solution flow, electric field, and presence of cations and anions in the solution: Au nanorods in AR deacetylation reaction as an example 25

11. The intraparticle catalytic communication distance x_0^{intra} and temporal memory t_0^{intra} are independent of experimental time resolution, segment size, catalytic activity, and fluorescence intensity threshold 27

11.1 They are independent of experimental time resolution within experimental error 27

11.2 They are independent of the segment length in dissecting the individual nanorods 28

11.3 They are independent of the nanorod's catalytic activity 29

11.4 They are independent of the fluorescence intensity threshold for selecting catalytic events on each nanocatalyst 29

12. Both intraparticle and interparticle catalytic communications are independent of the laser light power density, supporting that laser excitation and thus surface plasmon resonance of Au play insignificant roles 30

13. Applying voltage across the reactor cell using two Cu or Pt electrodes results in a steady-state electrical current, and they also cause similar changes in intra- and interparticle catalytic communication distances 31

14. Acetate and nitrite promote the reaction rates of Au-particle-catalyzed AR deacetylation and Rz deoxygenation, respectively, whereas resorufin does not 33

14.1 Ensemble reaction kinetics shows that the reaction product acetate and nitrite can promote the Au-particle-catalyzed reaction rates of AR deacetylation and Rz deoxygenation, respectively, whereas the product resorufin does not 33

14.2 Single-particle catalytic kinetics of Au nanorods also shows that acetate and nitrite can promote the catalytic rates of AR deacetylation and Rz deoxygenation, respectively 34

15. Other possible mechanisms of intraparticle catalytic communication and the many rationales against them 34

15.1 Reaction heat dissipation should not be the mechanism 34

15.2 Surface restructuring dynamics should not be the mechanism 36

15.3 Surface plasmon resonance of Au should not be the mechanism 36

16. Further discussions on the hole migration mechanism for intraparticle catalytic communications 37

16.1 Effective diffusion coefficient of hole migration for intraparticle catalytic communication 37

16.2 The positively-charged species should not be conduction band charges 38

16.3 Hole migration likely occurs via hole hopping, rather than atom migration 38

16.4 Proton is likely not the intra-particle catalytic messenger 39

16.5 Possible reasons for the non-operation of the molecular diffusion mechanism involving negatively-charged products for intra-particle catalytic communication 39

16.6 Strength of catalytic communication 40

17. 2-D analysis of ρ_{τ_i,τ_j} as a function of both Δx_{ij} and $\overline{\Delta t_{ij}}$ using a diffusive model for intraparticle catalytic communication 40

17.1 Formulation of 2-D diffusion model analysis 40

17.2 Delayed maxima are not expected to be observable for inter-particle catalytic communications. 42

18. Additional references 42

1. Synthesis and characterization of nanocatalysts

Pd nanorods and $mSiO_2$ coating. Pd nanorods were prepared using a hydrothermal synthesis following Huang et al.[1] All chemicals were purchased from Sigma-Aldrich unless specified otherwise. 17.7 mg $PdCl_2$, 300 mg NaI and 800 mg polyvinylpyrrolidone (PVP, MW = 55000) were dissolved in 18 mL nanopure water. Under stirring, the mixture was heated to 60 °C for 1 h in order to get a homogeneous solution and then transferred into a 100 mL Teflon-lined autoclave. The reactor was kept at 200 °C for 16 h to grow Pd nanorods. The resulting solution was cooled down to room temperature and mixed with isopropanol. The mixture was centrifuged at 10000 g for 10 min and then supernatant was removed. The washing and precipitation process was repeated once more. After purification, the precipitated Pd nanorods were collected and re-dispersed in 10 mL water for later silica shell overgrowth. The length and diameter of as-made Pd nanorods are 559 ± 223 nm and 37.4 ± 4.8 nm, respectively (Supplementary Figure 1a-d). According to Huang et al[1], these Pd nanorods are likely 5-fold twinned structure with five {100} side surfaces along the ⟨110⟩ direction.

The as-made Pd nanorods were coated by a mesoporous silica shell using a procedure slightly modified from that reported in our previous work[2]. There were three steps involved: shell growth, shell etching, and sample activation:

(1) Shell growth: 100 μL 0.11 M 3-mercaptopropionic acid (MPA) in ethanol (instead of MPTMS in reference[2]) was added to 10 mL Pd nanorod aqueous solution under stirring to replace the PVP left on Pd surface. After 24 h of this ligand exchange reaction, 100 μL 17 mM sodium silicate (Fisher Scientific) solution was added to grow an initial thin layer of silica on Pd nanorods. The resulting solution (pH adjusted to 9 using 2 M HCl solution) was stirred for 48 h and then centrifuged at 3,000 g to remove the supernatant. The precipitate was re-dispersed in a 10 mL 4:1 v/v ethanol/water mixture for the subsequent shell growth. 120 μL 10% (v/v) tetraethyl orthosilicate (TEOS) in ethanol and 100 μL 0.1 M NaOH solution were added into the mixture under vigorous stirring to grow a thick silica shell. After 24 h growth, the solution was centrifuged at 3,000 g, and the silica-coated Pd nanorods were collected. The silica shell thickness was ~150 nm. The silica-coated Pd nanorods were re-dispersed in 11:1 v/v water/ethanol mixture for etching the shell mesoporous.

(2) Shell etching: The above silica-coated Pd nanorod solution was mixed with 60 μL 0.1 M cetyltrimethylammonium bromide (CTAB) and 60 μL 0.1 M NaOH solutions. The mixture was stirred for 30 min and then heated at 90 °C for 40 min to form mesoporous silica (i.e., $mSiO_2$) coated Pd nanorods. The resulting solution was cooled to room temperature and centrifuged at 3,000 g to collect these nanorods as precipitate. The final sample was washed by water and ethanol multiple times and dried in air.

(3) Sample activation: The dried sample was calcinated in air at 450 °C for 1 h to remove organic compounds introduced in the synthesis and make the metal surface accessible to the reactant for catalytic reactions. After calcination (which also led to formation of palladium oxide), the $mSiO_2$-coated Pd nanorods were re-dispersed in 1 mL water. An adequate amount (~10 μL) of 0.1 M $NaBH_4$ solution was added drop-wise into the Pd nanorod solution until its color was changed from brown to gray and the solution was further kept for 5 min. (Note: too long an incubation in this solution would lead to a complete etch away of the shell.) The color change indicated that palladium oxide formed during calcination was reduced to Pd.[3] The sample after $NaBH_4$ treatment was washed by water multiple times to remove the unreacted $NaBH_4$. The final $mSiO_2$ shell thickness is ~125 nm, and the Pd nanorod cores maintain their rod morphology (Supplementary Figure 1e).

Au nanorods and nanoplates and $mSiO_2$ coating. Au nanorods were synthesized as we reported[2,4] (Supplementary Figure 1f), and are multiply twinned or single crystals[5-10]. The triangular- and hexagonal-shaped Au nanoplates were synthesized also as we reported[11,12] (Supplementary Figure 1h). The Au nanorods and nanoplates were then coated with a mesoporous silica shell (Supplementary Figure 1g, i) as we reported[2,11].

Necessity and advantage of the $mSiO_2$ coating. The $mSiO_2$ shell on Pd and Au nanocatalysts allows for subsequent calcination (or UV/ozone) treatment to remove the organic ligands on the metal surfaces for catalysis, while still maintaining the morphologies of nanorod and nanoplate cores and preventing their aggregation. This shell contains complex wormhole-like pores, which, according to literature, has an average pore size of ~3.5 nm and specific surface area of ~1000 $m^2\,g^{-1}$.[13] The reactants can still access the metal surface for catalysis through

the mesopores, and the mass transport of the reactants to the metal surface does not limit the catalytic kinetics as we demonstrated previously for $mSiO_2$-coated Au nanorods and nanoplates[2,11], primarily because the catalytic conversion kinetics is slow. The $mSiO_2$ shell also helps trapping the fluorescent product molecules temporarily (i.e., via molecular adsorption onto silica-based sites within the pores), facilitating their detection, as well as circumventing the potential fluorescence quenching associated with direct detection on metal surfaces.

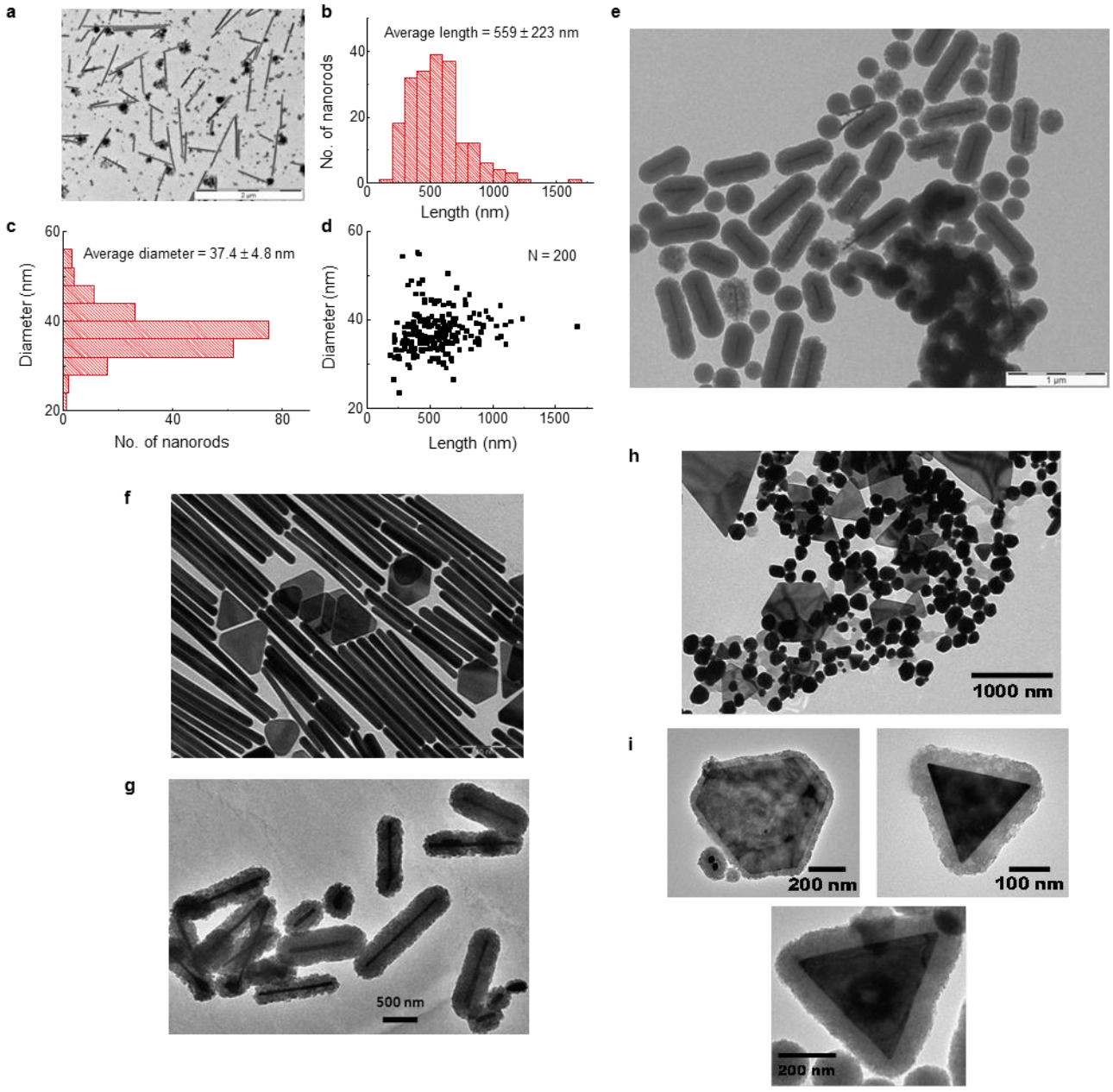

Supplementary Figure 1. Characterization of Pd nanorods, Au nanorods, and Au nanoplates before and after $mSiO_2$ coating. (**a-d**) TEM image (a) and the structural parameters of as-synthesized Pd nanorods. (**e**) TEM of the $mSiO_2$-coated Pd nanorods after $NaBH_4$ treatment. $mSiO_2$ shell thickness: 125.5 ± 6.5 nm. (**f-g**) TEM image of the as-synthesized (f) and $mSiO_2$-coated Au nanorods after heat treatment at ~500 °C (g). The nanorod sample also contains other shaped and many pseudospherical particles. The Au nanorods are about 100 to 700 nm in length and 21.4 ± 3.2 nm in diameter; the $mSiO_2$ shell is ~85 nm thick[2]. (**h-i**) TEM image of as-synthesized (h) and $mSiO_2$-coated Au nanoplates after UV/ozone treatment (i). The nanoplate sample is a mixture of Au nanoplates and pseudospherical particles. The nanoplates are triangular or hexagonal, with edge length of about 10 to 1000 nm and thickness of 13.7 ± 0.7 nm; the $mSiO_2$ shell is ~43

nm thick[11]. UV/ozone treatment was used instead of heat because heating to remove organic components changed the morphology of the Au nanoplate core.

2. Fluorogenic catalytic reactions, and ensemble assay shows that Pd nanorods can catalyze resazurin disproportionation to generate resorufin

Fluorogenic catalytic reactions. The three fluorogenic catalytic reactions are shown in Figure 1b in the main text. For most experiments, the reactant concentrations were such that the kinetics was saturated and pseudo-zeroth order to the reactant concentrations, and the kinetics was rate-limited by catalytic conversion from the reactants to the products rather than by reactant adsorption or product desorption, as we experimentally determined for Au nanocatalysts[2,11,14].

For Pd-nanorod-catalyzed photo-induced disproportionation of resazurin (Rz), the typical reaction conditions were: [Rz] = 0.05 μM in 10 mM pH 9.1 borate buffer. The reaction stoichiometry of resazurin to resorufin is ~3:1, determined from fluorescence measurement of the reaction solution (Supplementary Figure 2a). Previous studies have shown that under intense 532 nm excitation, photo-excited resazurin can disproportionate into a 1-electron reduced species and another 1-electron oxidized species[15], and the 1-electron reduced species can further disproportionate into resorufin, which is 2-electron reduced from resazurin, and resazurin[16]. We determined that the overall stoichiometry of this reaction without catalysis is also ~3:1 for resazurin to resorufin.

Regarding Au-based nanocatalysts, we have previously shown they can catalyze the oxidative deacetylation of AR by H_2O_2 and the reductive deoxygenation of Rz by NH_2OH. In both systems, the Au particle is the active catalyst component, while the $mSiO_2$ shell is not. For deacetylation, other reaction products include acetate and H_2O besides resorufin[17]. For deoxygenation, besides resorufin, another reaction product is nitrite (NO_2^-), which was detected by the colorimetric Griess reaction[18] and is consistent with the aqueous oxidative chemistry of NH_2OH[19]. The quantification of nitrite was done also by Griess reaction via calibration by standard solutions of potassium nitrite, giving a stoichiometry of resazurin to nitrite of ~2:1.

For AR deacetylation, the typical reaction conditions were (unless specified otherwise): [AR] = 0.2 μM, H_2O_2 kept at large excess at 60 mM, in 100 mM pH 7.2 phosphate buffer. At [AR] > ~0.2 μM, the reaction kinetics approaches pseudo-zeroth order to [AR] (and $[H_2O_2]$)[2]. For Rz deoxygenation, the reaction conditions were (unless specified otherwise): [Rz] = 0.2 μM, NH_2OH kept at large excess at 10 mM, in 100 mM pH 7.2 phosphate buffer. At [Rz] > ~0.15 μM, the reaction kinetics approaches pseudo-zeroth order to [Rz][11,14].

Ensemble activity assay of Pd nanorods (Supplementary Figure 2**).**

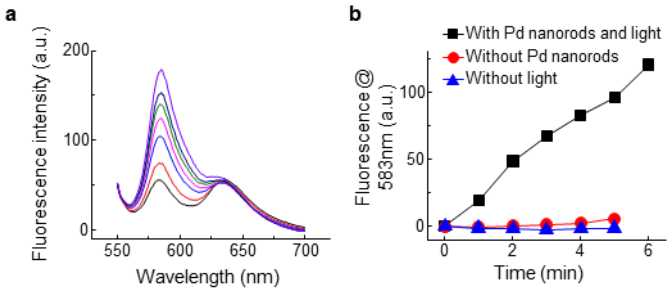

Supplementary Figure 2. Ensemble activity assay shows that Pd nanorods can catalyze the photo-driven disproportionation of resazurin to generate resorufin, while the un-catalyzed or non-illuminated reaction is negligible relatively. (**a**) Time-dependent fluorescence spectra of a reaction solution containing 86.4 μM resazurin, Pd nanorods and 0.2 M phosphate buffer under 5 mW 532 nm laser illumination (beam diameter = 0.7 mm). The ensemble measurements were done at pH = 7.2 to make the reaction faster and more easily measured, instead of pH 9.1 for single-molecule imaging measurements. The increase of fluorescence intensity peaked at 583 nm is due to the formation of resorufin. (**b**) Time profiles of fluorescence intensity at 583 nm of the reaction solution in **a** (black) and in control experiments similar to that in **a** except that no Pd nanorods were added (red) or no 532 nm laser illumination (blue). The reaction rate is 0.35 ± 0.10 μM/min for Pd-catalyzed disproportionation (black), 0.019 ± 0.024 μM/min for the uncatalyzed

disproportionation (red) and zero (i.e., –0.004 ± 0.016 μM/min) without 532 nm illumination (blue). **Methods:** Since the as-synthesized Pd nanorods are capped by PVP, they cannot be used directly as catalysts. We thus used the surfactant-free Pd nanorods to test their ensemble catalytic activity. The heat-treated $mSiO_2$-coated Pd nanorods were dispersed in 0.1 M $NaBH_4$ and the mixture was kept for 3 h to reduce the palladium oxide formed in calcination as well as to dissolve the $mSiO_2$ shell (due to the strongly basic $NaBH_4$ solution), which exposed more Pd surfaces for ensemble activity measurements. The Pd nanorods were collected by centrifugation. The reaction solution was sealed in a borosilicate glass tube (Sutter Instrument) for the ensemble activity measurement.

3. Experimental setup for single-molecule fluorescence imaging, solution flow and voltage manipulations, as well as acetate and nitrite effects

Experimental setup for single-molecule fluorescence imaging. Catalysis on individual nanocatalysts was imaged using single-molecule fluorescence microscopy[2,20-31], based on a total internal reflection fluorescence microscope, at room temperature under ambient conditions (Supplementary Figure 3), as described[2,11]. A continuous-wave circularly polarized 532 nm laser of 2-30 mW induced the fluorescence of the product resorufin generated on immobilized nanocatalysts within an area of ~50 × 100 μm^2 on a slide in a microfluidic reactor (dimension: ~150 μm high, ~5 to 10 mm wide, and ~3 cm long, formed by double-sided tape sandwiched between a quartz slide and a coverslip). The aqueous reactant solution was supplied into the reactor continuously at 5 to 100 $\mu L\ min^{-1}$, which provided a steady-state reaction condition. The fluorescence of the product resorufin was imaged at the single-molecule level and recorded by an EMCCD camera operating at 25 or 30 ms frame rate.

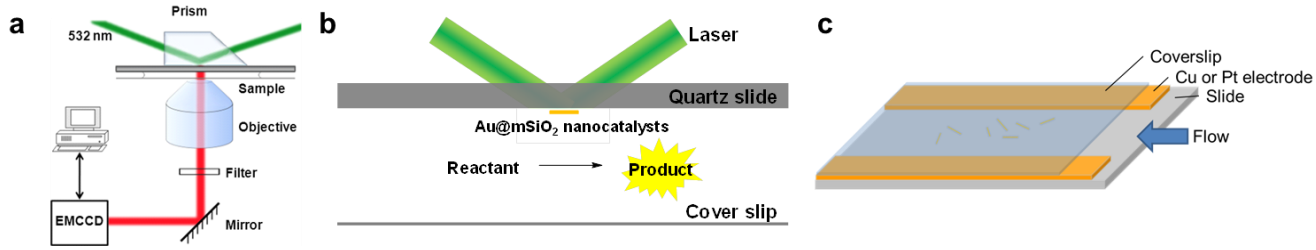

Supplementary Figure 3. Single-molecule fluorescence imaging of catalysis. (**a**) Experimental scheme using a homebuilt prism-based total internal reflection (TIR) fluorescence microscope (Olympus IX71) with 532 nm laser excitation and a liquid microfluidic reactor cell made between a quartz slide and a cover slip. Figure adopted from our previous publication[2]. (**b**) Schematic of the microfluidic reactor cell (approximately 150 μm (height), 3 cm (length), and 5-10 mm (width)) showing catalyst particles immobilized on the slide, the fluorogenic catalytic reaction, and the TIR laser excitation. (**c**) Schematic of the microfluidic reactor construction for voltage manipulation experiments. The two metal electrodes (copper foil or platinum wire) are sandwiched between the quartz slide and the coverslip, held together by double-sided tapes. The distance between the two electrodes is 5-8 mm.

Solution flow and voltage manipulations. The reactant solution flow was varied from ~5 to 100 $\mu L\ min^{-1}$ using a syringe pump, corresponding to a linear flow rate of ~100 to 2000 $\mu m\ s^{-1}$ (depending on the cross section of the particular reactor). A two-electrode configuration potentiostat was used to apply a voltage ranging from –1.2 to 1.2 V across the microfluidic reactor (see SI Section 13 for more details).

The interparticle and intraparticle *i*-to-*j* vector orientation angles are defined in Figure 4a relative to the solution flow (θ) and the EF direction (φ). In analyzing the dependence of the catalytic communication distance on the orientation angle (e.g., Figure 5b and e), the data were fitted with the following cosine function:

$$y = a\cos x + b \qquad (1)$$

where x is either θ or φ; a is the amplitude of the cosine function (e.g., $\Delta x_{0,\mathrm{flow}}^{\mathrm{inter}}$ and $\Delta x_{0,\mathrm{EF}}^{\mathrm{inter}}$ in Figure 5c and f), which could be positive or negative; and b is an offset.

Acetate and nitrite effects. Various concentrations of acetate and nitrite were titrated into the reaction solution for the Au-nanocatalyst catalyzed AR deacetylation and Rz deoxygenation, respectively. See data in SI

Section 14. The promotion effect on the catalytic activity by acetate or nitrite (e.g., Figure 5g) was fitted with the following saturation equation:

$$y = \frac{ax}{x + K_{1/2}} + b \quad (2)$$

where x is either [CH_3COO^-] or [NO_2^-], and $K_{1/2}$ is the half-saturation concentration of added acetate or nitrite. The corresponding quenching effect of acetate or nitrite on the interparticle catalytic communication distance (e.g., Figure 5h) was fitted with a negative saturation equation:

$$y = -\frac{ax}{x + K_{1/2}} + b \quad (3)$$

4. Data processing for single-molecule fluorescence imaging, localization precision, and spatial resolution

The fluorescence signals of the products during catalytic reactions were imaged at the single-molecule level and recorded in a movie. We analyzed the movie images to localize the positions of individual product molecules, as similarly done in STORM[30,32] and PALM[29,31,33], two closely related super-resolution imaging techniques based on wide-field single-molecule fluorescence detection. The analysis was done using a home-written MATLAB program[2]. Exemplary data of individual product position maps are presented in Supplementary Figure 4f, h, and j. Our analysis procedures were described in detail previously[2], and summarized schematically in Supplementary Figure 4 and below.

Localization precision and spatial resolution of 30-40 nm. We typically localize the positions of individual fluorescent product resorufin on individual nanocatalysts to about 35-45 nm precision, in correlation with the nanocatalyst's SEM image. This 35-45 nm uncertainty includes contributions from the signal/noise ratio of single-molecule fluorescence imaging, and is comparable to the potential influence from the fluorescence scattering by the plasmonic Au nanorods/nanoplates that could potentially shift the fluorescence central position by tens of nanometers[34-36]. Using different-diameter pseudospherical $mSiO_2$-coated Au nanoparticles, we previously showed that the typical spatial resolution of our method is 30-40 nm, reflected by the fact that this super-resolution catalysis imaging can accurately measure the diameter of pseudospherical Au nanocatalysts down to 30-40 nm[37]. *Note that this spatial resolution is much smaller than the segment size in dissecting Pd/Au nanorods and nanoplates in our analysis of catalytic communications as well as much smaller than the intraparticle catalytic communication distance* x_0^{intra}.

Summary of analysis procedure. First, we identified the individual nanocatalysts in both the SEM (Supplementary Figure 4d-1) and the optical/fluorescence images (Supplementary Figure 4d-3 and d-6); these nanocatalysts scatter laser light strongly, and are also emissive (for Au nanocatalysts) (Supplementary Figure 4d-3), and thus readily identifiable in the optical microscope. We then extracted the fluorescence intensity trajectory of each nanocatalyst under catalysis from the recorded fluorescence movie by integrating the EMCCD counts over a 7×7 pixel area (each pixel ~267 nm) around the nanorod/nanoplate (Supplementary Figure 4a-1 and b). The trajectory showed bursts of fluorescence intensity on top of the background emission signal of the nanorod/nanoplate itself; the bursts are due to catalytic formations of the product molecule resorufin. We then used intensity thresholds to select the fluorescence burst events from product molecule formation (Supplementary Figure 4a-2). An area of 13 × 13 pixels (~3.5 ×3.5 μm^2) around the product molecule was cropped out, and all image frames contributing to the same single burst were added together to enhance the signal to noise ratio (Supplementary Figure 4a-3). From this image, the emission/background signal of the nanocatalyst itself was subtracted; here the nanocatalyst emission signal was taken from the image frames right before the appearance of the burst signal in the movie. The resulting image only contained the fluorescence signal of the catalytic product molecule resorufin. Then the image of the molecule, which behaves as a point spread function (PSF), was fitted by a two-dimensional

Gaussian function to obtain the center position (x_0, y_0) of the PSF, which reflects the position of the product molecule (Supplementary Figure 4a-4 and c). Provided that a large number of fluorescence photons are detected, the center position (x_0, y_0) can be localized down to a few nm accuracy[38,39], but often around 35-45 nm in this study due to a short residence time of the product on the nanocatalyst. To reduce the contribution of noises to the selected burst events, we further filtered the selected burst events by their localization accuracies and the widths of the fitted PSF (Supplementary Figure 4a-5), as we described previously[2]. The center positions of all molecules were further corrected for microscope stage drifting, using the intrinsic emission signal of the Au nanoparticles as position markers (Supplementary Figure 4a-6).

The positions of catalytic product molecules on a single nanocatalyst can be overlaid together in a scatter plot (Supplementary Figure 4a-7 and d-4) and correlated with the SEM image of the nanocatalyst (Supplementary Figure 4a-8 and d-1), whose structural contour was determined from the SEM image. The correlation with the SEM image could be directly mapped using position markers, as we described[2,11], and for the nanorods, could also be performed by fitting the SEM structural contour to the 2-D histogram of the product positions as we demonstrated (Supplementary Figure 4d-5)[2]. Once the structural contour of a nanocatalyst was mapped on top of the positions of catalytic products, the nanocatalyst could be dissected into segments. The product molecules were sorted to their corresponding segments, on the basis of their positions.

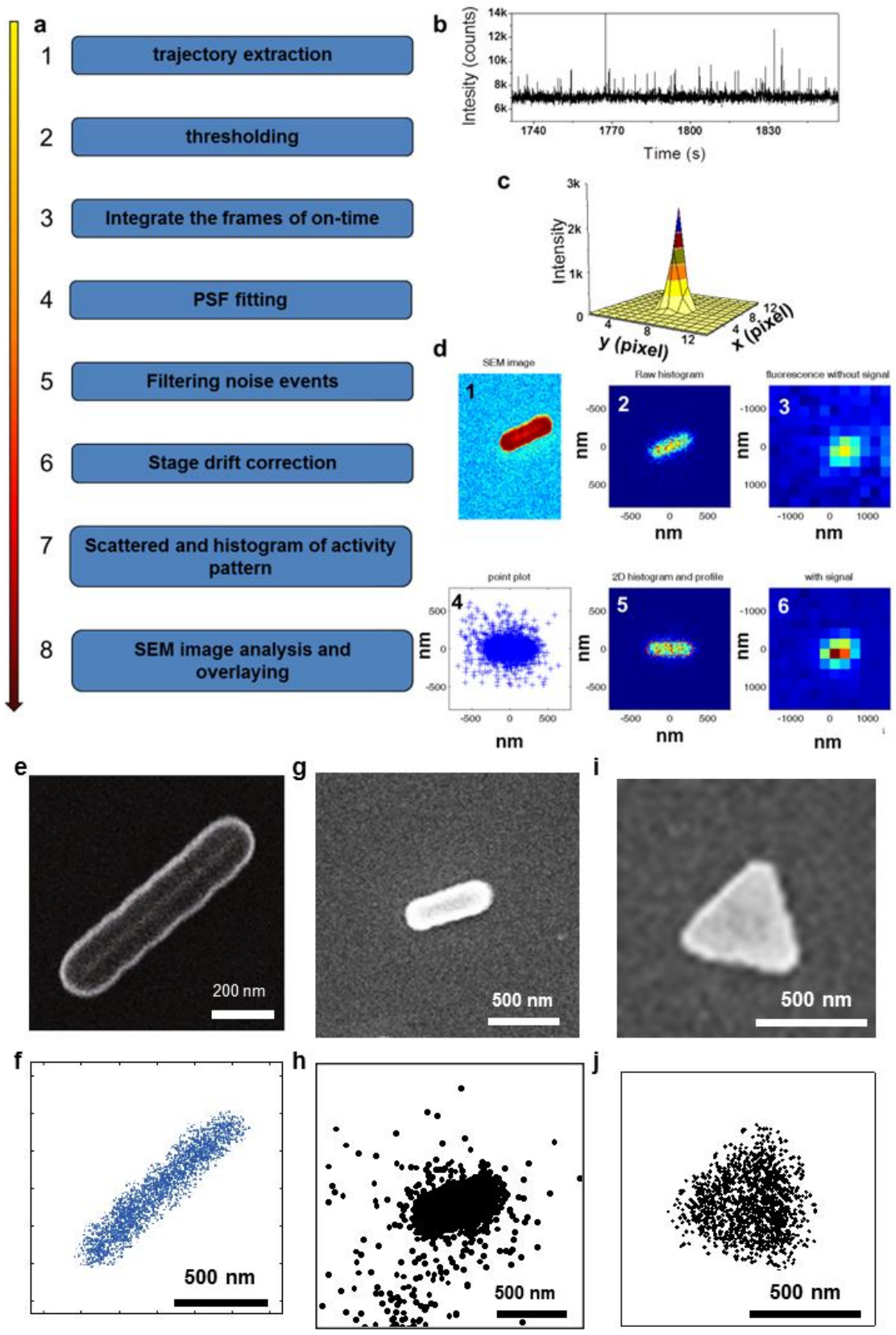

Supplementary Figure 4. Scheme of single-molecule super-resolution imaging analysis of catalytic reactions (a-d) and exemplary data on single Pd and Au nanocatalysts (e-j). (**a**) Major analysis steps for super-resolution imaging of

the catalytic products on individual nanocatalysts. (**b**) A fluorescence intensity trajectory from a $mSiO_2$-coated Au nanorod undergoing catalysis; the fluorescence intensity bursts are due to the formation events of the catalytic product resorufin. (**c**) 2-D Gaussian fitting of the PSF of a fluorescent product on a Au nanorod. (**d**) Exemplary data: (1) SEM image of a $mSiO_2$-coated Au nanorod; (2) 2-D histogram of product positions as in (4) on the nanorod shown in (1). (3) The emission signal/image of the nanorod in (1). (4) Scatter plot of the positions of the many product molecules detected on the nanorod in (1). (5) 2-D histogram of (4) with the SEM structural contour from (1) overlaid on top; note that the orientations of both (4) and (5) are rotated relative to those of (1) and (2) so that the long axis of the nanorod lies horizontally. (6) The fluorescence signal/image of a resorufin product on top of the nanorod. (**e**) SEM of the Pd nanorod, same as Figure 1c in the main text. (**f**) Positions of many product P molecules from the disproportionation of resazurin on the nanorod in **e**, from which the 2-D histogram in Figure 1d was obtained. Each dot is one P molecule. (**g**) SEM of a $mSiO_2$-coated Au nanorod. (**h**) Positions of many product P molecules from the deacetylation reaction of amplex red detected on the nanorod in **g**. (**i**) SEM of a triangular $mSiO_2$-coated Au nanoplate presented in Supplementary Figure 17a. Note that the orientation of Supplementary Figure 17a has been rotated so that one edge of the nanoplate aligns horizontally. (**j**) Positions of many P molecules from the deoxygenation reaction of resazurin detected on the nanoplate in **i**.

5. The product resorufin stays on the nanorod for ~38 ms on average, orders of magnitude shorter than its photoblinking/bleaching on-time, and it stays essentially stationary within our localization precision before desorbing into solution

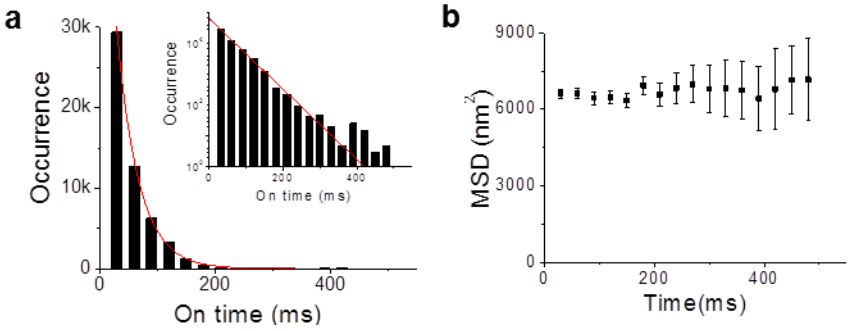

Supplementary Figure 5. (**a**) Distribution of the fluorescence on-time (i.e., the time each product molecule stays adsorbed on the nanocatalysts) for Au nanorod catalyzed AR deacetylation reaction, as an example. It follows a single exponential distribution (red line) with **a time constant 37.9±0.6 ms, which is <2 imaging frames and is ~2 orders of magnitude shorter than the photobleaching/blinking on-times of the product resorufin that occur at seconds or longer timescales**[14,40]. Inset: same plot in log-linear scale, showing that some *individual* on-times can be a few hundred ms long, which allows us to track the position of the product molecule frame-by-frame while it stayed adsorbed on the nanocatalyst. **(b)** Mean-square-displacement (MSD, $\langle r^2 \rangle = \langle (x_i - x_j)^2 + (y_i - y_j)^2 \rangle$) vs time of the product resorufin during the fluorescence on-times by tracking the position of the individual resorufin product during each fluorescence on-time. The MSD does *not* increase with increasing time, **indicating that the resorufin stays essentially stationary and does not diffuse much laterally within the $mSiO_2$ shell before it desorbs into the surrounding solution**. This stationary behavior likely comes from resorufin adsorption onto sites in the mesopores of the $mSiO_2$ shell, at which desorption into solution is faster than diffusing along the nanorod's long axis within the $mSiO_2$ shell laterally. The finite positive value of MSD (i.e., $\langle r^2 \rangle$~6500 nm^2) comes from the fact that the x and y positions of each product molecule have a localization uncertainty of ~40 nm. This localization uncertainty can be described by a Gaussian distribution of x and y, $P(x)$ and $P(y)$, centered at the true positions x_0 and y_0 with a standard deviation σ of ~40 nm: $P(x) = \frac{1}{\sigma\sqrt{2\pi}} e^{-\frac{(x-x_0)^2}{2\sigma^2}}$ and $P(y) = \frac{1}{\sigma\sqrt{2\pi}} e^{-\frac{(y-y_0)^2}{2\sigma^2}}$. The expected value of r^2 is then $E(r^2) = E\left((x_i - x_j)^2 + (y_i - y_j)^2\right) = \iint (x_i - x_j)^2 P(x_i)P(x_j)\mathrm{d}x_i\mathrm{d}x_j + \iint (y_i - y_j)^2 P(y_i)P(y_j)\mathrm{d}y_i\mathrm{d}y_j = 4\sigma^2$. As $\sigma \sim$ 40 nm, the expected value of r^2 is ~6400 nm, consistent with the experimental observation here.

6. Analysis procedures of the *intra-* and *inter-particle* catalytic communications between temporally subsequent reactions that occur at different locations

6.1 Intraparticle catalytic communication within Pd or Au nanorods

Once we obtained the catalytic event sequence of each nanorod segment, we analyzed the correlation of the microscopic reaction time τ between temporally subsequent reactions that occur at different segments. For any segment i on a single nanorod that has many catalytic events (i = 1 to n; n is the total number of segments of a nanorod), the microscopic reaction time τ_i of each event is paired with τ_j of the *immediate subsequent* catalytic event that occurs on a different segment j (j = 1 to n; $j \neq i$) on the same nanorod (Supplementary Figure 6a, b). In this way, we obtained many $\tau_i \rightarrow \tau_j$ pairs between the event sequence of segment i and that of segment j. A Pearson's cross-correlation coefficient ρ_{τ_i,τ_j} was then calculated for these *many* $\tau_i \rightarrow \tau_j$ pairs (implemented in MATLAB using the built-in function "corrcoef"):

$$\rho_{\tau_i,\tau_j} = \frac{\langle \tau_i \tau_j \rangle - \langle \tau_i \rangle \langle \tau_j \rangle}{\sqrt{\left(\langle \tau_i^2 \rangle - \langle \tau_i \rangle^2\right)\left(\langle \tau_j^2 \rangle - \langle \tau_j \rangle^2\right)}} = \frac{m\sum_m \tau_i \tau_j - \sum_m \tau_i \cdot \sum_m \tau_j}{\sqrt{\left[m\sum_m \tau_i^2 - \left(\sum_m \tau_i\right)^2\right] \cdot \left[m\sum_m \tau_j^2 - \left(\sum_m \tau_j\right)^2\right]}} \quad (4)$$

Here m is the number of $\tau_i \rightarrow \tau_j$ pairs and $\langle\ \rangle$ denotes averaging. Note that this event pairing is directional and asymmetric between the segment i and j: it uses all τ_i's in the event sequence from segment i, except for its last event, which may or may not have a subsequent event on sequence j; but not all τ_j's of the event sequence j are necessarily used. Our analysis computed the cross-correlation coefficient for both directions when both i and j are stepped from 1 to n. ρ_{τ_i,τ_j} is a quantitative measure of how the catalytic kinetics, reflected by τ, of any reaction on one segment is correlated with the temporally subsequent one at another segment on the same nanorod. Each ρ_{τ_i,τ_j} is also a statistical property averaged over the many pairs of temporally subsequent catalytic events, in which the pairs all have the distance separation Δx_{ij} between the two segments i and j, defined as the center-to-center distance between the two segments.

For each $\tau_i \rightarrow \tau_j$ pair, the event associated with τ_j occurred at a certain time after that associated with τ_i, i.e., there is a time delay Δt_{ij} between these two temporally subsequent events that occur at two different segments. By averaging all Δt_{ij}, we obtained $\overline{\Delta t_{ij}}$, the average time separation between any two temporally subsequent events that occurred on the two segments i and j. Each ρ_{τ_i,τ_j} is thus also associated with an average time separation, $\overline{\Delta t_{ij}}$, besides a distance separation, Δx_{ij}. **Overall, ρ_{τ_i,τ_j} is a function of Δx_{ij} and $\overline{\Delta t_{ij}}$, i.e., $\rho_{\tau_i,\tau_j}\left(\Delta x_{ij}, \overline{\Delta t_{ij}}\right)$.** The value of ρ_{τ_i,τ_j} can be between −1 and 1. If τ_i and τ_j are completely correlated, ρ_{τ_i,τ_j} = 1; if completely uncorrelated, ρ_{τ_i,τ_j} = 0; if completely anticorrelated, ρ_{τ_i,τ_j} = −1.

The obtained ρ_{τ_i,τ_j} between many segments from many nanorods are pooled together to increase statistics, binned along the dimension of Δx_{ij} or $\overline{\Delta t_{ij}}$, and then averaged within each bin, so as to obtain the dependence of ρ_{τ_i,τ_j} on Δx_{ij} or $\overline{\Delta t_{ij}}$, for example as presented in Figure 2a-b in the main text.

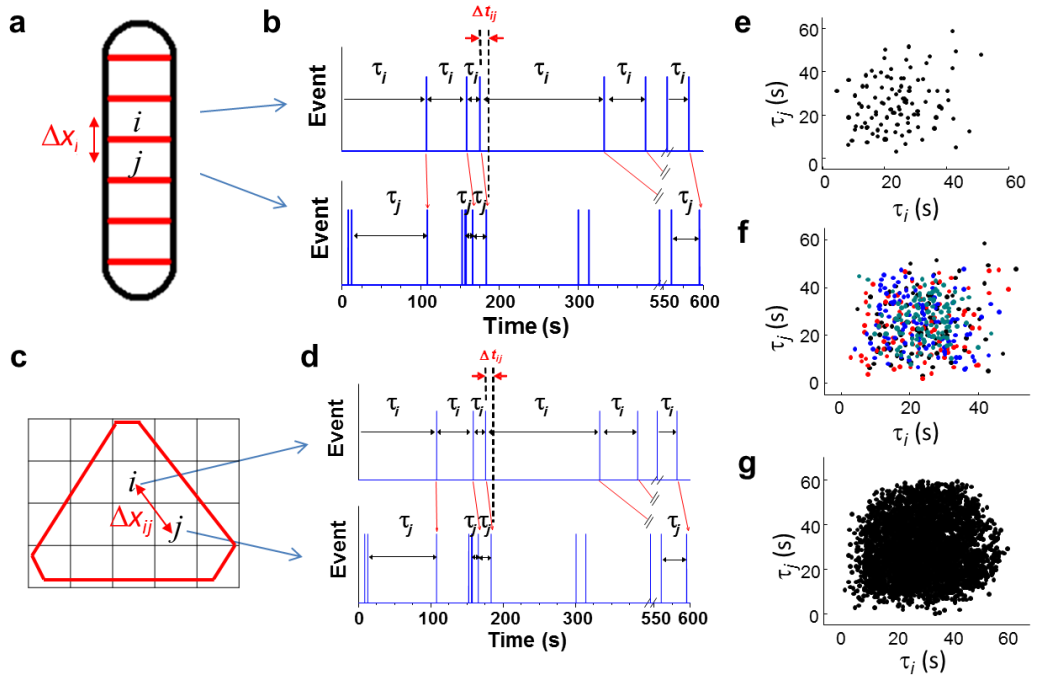

Supplementary Figure 6. Spatiotemporally dependent cross-correlation analysis of the microscopic reaction time τ between temporally subsequent reactions that occur on two different segments on a single nanorod (a-b) or nanoplate (c-d). (**a**) Schematic of dissecting a nanorod into segments. (**b**) Schematic of two catalytic event sequences, each from a single segment. In each sequence, the individual product formation events (vertical lines) were plotted against the times when they were detected. The microscopic reaction time τ for each event is the time separation from the previous one in the same sequence. Pairs of reactions that are temporally subsequent but occur at different segments are linked by red arrows. The time separation (Δt_{ij}) was shown for one pair of catalytic events, each occurring at one of the two segments. (**c-d**) Same schematics as a-b, but for a nanoplate, which is dissected into square segments. (**e**) Exemplary scatter plot of τ_i vs. τ_j from one pair of two neighboring segments from a single Pd nanorod in catalyzing the disproportionation reaction; $\rho = 0.23$ here. (**f**) Same as e, but from 4 pairs of neighboring segments from a single Pd nanorod dissected into 5 segments. $\rho = 0.16$, averaged over the 4 pairs. (**g**) Same as e, but are compiled from >230 segments of >40 Pd nanorods. $\rho = 0.08$.

6.2 Intraparticle catalytic communication within Au nanoplates

For the pseudo-2-D nanocrystal Au nanoplates, we dissected each nanoplate into square segments of 100 - 200 nm in each dimension (Supplementary Figure 6c). Depending on the nanoplate, the size of the square segments was varied so that there were appreciable amount catalytic events in each segment. Most segments have more than 40 events. (The segments near the edges and corners of a nanoplate are not squares, and sometimes they are so small that there are less than 40 events in it; these edge/corner segments were thus excluded in the analysis.) From each segment, we obtained its time sequence of catalytic events (Supplementary Figure 6d). We then calculated ρ_{τ_i,τ_j} between any two segments of every Au nanoplate, and pooled all ρ_{τ_i,τ_j} from many nanoplates together.

6.3 Interparticle catalytic communication between temporally subsequent reactions that occur on different particles

For interparticle analysis, Pearson's cross-correlation coefficient ρ_{τ_i,τ_j} was calculated between temporally subsequent reactions that occur on *different* nanorods or nanoplates. Two effectively same methods were used in calculating the interparticle ρ_{τ_i,τ_j}. In one method, the ρ_{τ_i,τ_j} was calculated between the real-time catalytic event sequences of two segments, each belonging to a different nanorod or nanoplate (i.e., the segment-to-segment method). In the alternative method, the real-time sequences of catalytic events were generated for the individual nanocatalysts as a whole, and then calculate ρ_{τ_i,τ_j} between any two nanorods or nanoplates (i.e., the particle-to-

particle method). In both methods, each ρ_{τ_i,τ_j} is also associated with an interparticle distance separation (Δx_{ij}) and an average time separation $\overline{\Delta t_{ij}}$ between any two temporally subsequent events that occur on two different segments/particles. Supplementary Figure 7 shows the results for Au nanorods catalyzing the deacetylation reaction. In both methods, the ρ_{τ_i,τ_j} vs. Δx_{ij} or $\overline{\Delta t_{ij}}$ dependencies are indistinguishable within experimental error. As the particle-to-particle method allows for analyzing the data from pseudospherical particles that were also present in the sample of Au nanorods/nanoplates and that could not be segmented due to their smaller size (Supplementary Figure 1f-i), the particle-to-particle method allows for more statistics. We thus used the particle-to-article method for all later analysis of interparticle catalytic communications.

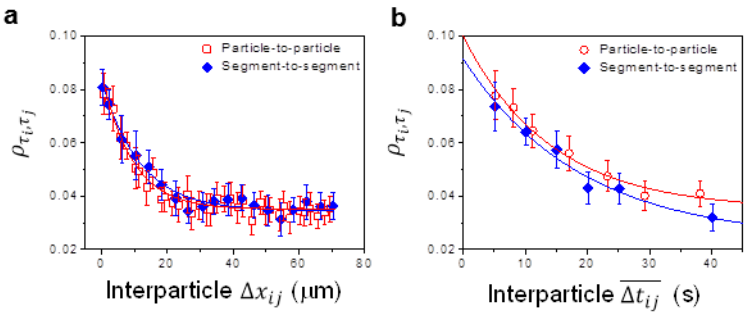

Supplementary Figure 7. Segment-to-segment and particle-to-particle analysis of interparticle catalytic communication between Au nanorods (and pseudospherical particles) in catalyzing the deacetylation reaction. (**a, b**) Cross-correlation coefficient ρ_{τ_i,τ_j} for interparticle catalytic communication vs. interparticle Δx_{ij} or $\overline{\Delta t_{ij}}$. Solid lines are single exponential fits with a *y*-offset, which is the limiting value at long distance and time separations and represents the spurious contribution. For the segment-to-segment analysis method, x_0^{inter} = 10.2 ± 2.6 μm and t_0^{inter} = 16.2 ± 3.6 s; for the particle-to-particle analysis method, x_0^{inter} = 11.7 ± 2.0 μm and t_0^{inter} = 18.9 ± 2.8 s; both methods yield essentially the same results.

6.4 Spurious contributions to cross-correlation coefficients, reflected by the interparticle ρ_{τ_i,τ_j} at long distance and time separations, are used as a residual offset for the intraparticle ρ_{τ_i,τ_j}

For interparticle cross-correlation coefficient ρ_{τ_i,τ_j}, it decays exponentially with increasing interparticle Δx_{ij} or $\overline{\Delta t_{ij}}$, but it does not decay to zero, and instead to a limiting residual value at long distance and time separations (e.g., Supplementary Figure 7). This residual cross-correlation varies slightly (0.034 ± 0.009) depending on the particular catalytic reaction and the different batches of samples. This residual cross-correlation is also present when the catalytic events are randomized spatially, temporally, or both (Supplementary Figure 9c-d); and it is also present in the simulated random catalytic events (Supplementary Figure 11h-i). Therefore, this residual cross-correlation represents spurious contributions to the calculated ρ_{τ_i,τ_j}, and it was used as a fixed residual offset in fitting exponential functions to all intraparticle ρ_{τ_i,τ_j} vs. Δx_{ij} or $\overline{\Delta t_{ij}}$ results, which, due to the particle size limit, does not have values at long intraparticle distance separations.

6.5 Additional discussions on the reliability of the correlation analyses for demonstrating the intra- and inter-particle catalytic communication

The catalytic communications we observed are in general weak, i.e., small positive correlations that would typically be outside the confidence level of correlation analysis. However, we are confident about the observed phenomena of catalytic communications and the conclusions because of the following:

1) First of all, our conclusions are not based on the "absolute" magnitudes of the spatiotemporal cross correlations, but on "trends" of how the correlations depend on distance separation and time separation of single catalysis events, and on solution flow direction and rate, voltage direction and amplitudes, and concentrations of

externally added ions. These trends across multiple catalyst and reaction systems are the strong base of the reliability of our results and conclusions.

2) A residual correlation at limiting distance and time of infinity was present. It is a spurious contribution, because the same residual correlation could be reproduced when the experimental data of single reaction events are randomized in spatial location, temporal sequence, or both (e.g., Figure 2a-b, blue lines and Supplementary Note 7), or when using simulated random events (Supplementary Note 8). Moreover, the correlations from these randomization and simulation controls do not show a decay with increasing distance and time separations, in contrast to the actual data.
3) We do have experimental examples of larger, more significant correlations:
    a) The Au-nanorod catalyzed resazurin reduction reaction: its intra-particle catalytic communication has a correlation amplitude of 0.213 ± 0.045 (Supplementary Figure 15a-b and Supplementary Table 2).
    b) The Au-nanoplate catalyzed resazurin reduction reaction: its inter-particle catalytic communication has a correlation amplitude of 0.18 ± 0.06 (Supplementary Figure 17d-e and Supplementary Table 2).

    Unfortunately, we currently do not have a quantitative understanding of what determines the amplitude (i.e., strength) of the correlations, other than stating "stronger or weaker" on the basis of the experimentally observed variations of amplitude values. Future research, perhaps via theoretical modeling, is needed.
4) We also have a negative example: The Pd-nanorod catalyzed disproportionation reaction does not show inter-particle catalytic communication; we rationalized it by that this reaction lacks such anion products as acetate and nitrite. This negative example establishes that our data analysis procedure is not the reason for the observed correlations of other cases.
5) The amplitudes of correlation in our analysis are expected to be smaller than the overall strength of the catalytic communications because our computed cross correlation coefficient is for temporally subsequent reactions between any "two" segments, whereas the catalytic messenger, either the proposed surface localized hole or a product anion, could migrate from one segment to *any other* segment on the same particle or to *any other* particle, for the intra- and inter-particle communications, respectively. If the correlation is summed over all possible segments, its numerical value would be significantly larger. For example, for the intra-particle catalytic communication of Pd-nanorod-catalyzed disproportionation reaction in Figure 2a (red curve), the summation over all intra-particle distance separation would give an overall correlation of ~0.18 (the residual correlation values are excluded here) .

7. Both intra- and inter-particle catalytic communication behaviors vanish if the temporal sequence, spatial locations, or both of the catalytic events on each nanocatalyst are randomized

For a single particle (or a segment), the detected catalytic product formation events occur one at a time, each associated with a microscopic reaction time τ, which is the time separation from the previous event on the same particle (or segment), and with a location (x,y) where this event occurred. For the n'th event (n is the event index), the absolute time t this event occurred is equal to $\sum_{m=1}^{n} \tau_m$. When we analyzed the cross-correlation coefficient of the microscopic reaction time (τ) between temporally subsequent reactions that occur at different segments on the same particle (i.e., intraparticle) or on different particles (i.e., interparticle), we paired the microscopic reaction time τ of each catalytic event on one segment (or particle) with the microscopic reaction time τ of the immediate subsequent catalytic event that occurs on another segment (or particle). In this way, we obtained many τ-pairs between two segments of the same particle or between two different particles, and then computed the Pearson's cross-correlation coefficient of these catalytic events in *both temporally and spatially defined manner*.

As this cross-correlation coefficient is related to the temporal sequence and spatial locations of individual catalytic reactions, we expected that the correlation, i.e., catalytic communication behavior, would vanish, if we artificially randomize the temporal sequence, spatial locations, or both of the individual reaction events. To randomize the temporal sequence of the catalytic events, we randomly changed the temporal order of catalytic events, for each of which its τ and location (x, y) are maintained (Supplementary Figure 8a). To randomize the spatial locations, we randomly swapped the locations of individual events, for each of which its τ and temporal sequence and thus its absolute occurring time are maintained (Supplementary Figure 8b). To randomize both the

temporal sequence and spatial locations, we randomly changed the temporal order of each τ, but left the locations in the same order so that for each τ, it has a different location and different occurring time (Supplementary Figure 8c). All these event randomizations do not change the average turnover rate of the particle (or segment), as we do not change the total number of events on each segment (or particle).

a. temporal randomization

Events Index	X_0(nm)	Y_0(nm)	τ(s)	Accumulative Time (s)
1	-62.54	399.17	3.88	3.88
2	-303.9	435.67	2.36	6.24
3	151.38	786.63	9.305	15.545
4	211.51	770.89	2.91	18.455
5	126.17	814.6	0.035	18.49
6	-109.8	350.2	3.13	21.62
7	-268.9	504.21	2.485	24.105
8	-367.3	437	0.025	24.13
9	1502.4	6.35	4.32	28.45
10	179.05	932.72	1.325	29.775
11	248.81	930.1	5.9	35.675
12	141.46	800.88	21.275	56.95
13	645.46	-654.9	8.295	65.245
14	108.82	915.56	16.995	82.24
15	122.46	1102.7	0.265	82.505
16	9.36	1138.5	2.93	85.435
17	112.89	983.15	2.075	87.51
18	113.02	1146.5	2.32	89.83
19	-259	520.58	2.93	92.76
20	221.36	619.19	0.235	92.995

Events Index	X_0(nm)	Y_0(nm)	τ(s)	Accumulative Time (s)
1	-109.8	350.2	3.13	3.13
2	151.38	786.63	9.305	12.435
3	9.36	1138.5	2.93	15.365
4	248.81	930.1	5.9	21.265
5	-268.9	504.21	2.485	23.75
6	112.89	983.15	2.075	25.825
7	108.82	915.56	16.995	42.82
8	-367.3	437	0.025	42.845
9	126.17	814.6	0.035	42.88
10	-259	520.58	2.93	45.81
11	122.46	1102.7	0.265	46.075
12	-62.54	399.17	3.88	49.955
13	-303.9	435.67	2.36	52.315
14	211.51	770.89	2.91	55.225
15	113.02	1146.5	2.32	57.545
16	645.46	-654.9	8.295	65.84
17	1502.4	6.35	4.32	70.16
18	221.36	619.19	0.235	70.395
19	179.05	932.72	1.325	71.72
20	141.46	800.88	21.275	92.995

b. spatial randomization

Events Index	X_0(nm)	Y_0(nm)	τ(s)	Accumulative Time (s)
1	-62.54	399.17	3.88	3.88
2	-303.9	435.67	2.36	6.24
3	151.38	786.63	9.305	15.545
4	211.51	770.89	2.91	18.455
5	126.17	814.6	0.035	18.49
6	-109.8	350.2	3.13	21.62
7	-268.9	504.21	2.485	24.105
8	-367.3	437	0.025	24.13
9	1502.4	6.35	4.32	28.45
10	179.05	932.72	1.325	29.775
11	248.81	930.1	5.9	35.675
12	141.46	800.88	21.275	56.95
13	645.46	-654.9	8.295	65.245
14	108.82	915.56	16.995	82.24
15	122.46	1102.7	0.265	82.505
16	9.36	1138.5	2.93	85.435
17	112.89	983.15	2.075	87.51
18	113.02	1146.5	2.32	89.83
19	-259	520.58	2.93	92.76
20	221.36	619.19	0.235	92.995

Events Index	X_0(nm)	Y_0(nm)	τ(s)	Accumulative Time (s)
1	141.46	800.88	3.88	3.88
2	-109.77	350.2	2.36	6.24
3	645.46	-654.94	9.305	15.545
4	-303.85	435.67	2.91	18.455
5	248.81	930.1	0.035	18.49
6	179.05	932.72	3.13	21.62
7	122.46	1102.67	2.485	24.105
8	9.36	1138.47	0.025	24.13
9	-62.54	399.17	4.32	28.45
10	113.02	1146.49	1.325	29.775
11	126.17	814.6	5.9	35.675
12	108.82	915.56	21.275	56.95
13	-268.91	504.21	8.295	65.245
14	151.38	786.63	16.995	82.24
15	1502.43	6.35	0.265	82.505
16	-259.03	520.58	2.93	85.435
17	211.51	770.89	2.075	87.51
18	221.36	619.19	2.32	89.83
19	-367.26	437	2.93	92.76
20	112.89	983.15	0.235	92.995

c. spatial and temporal randomization

Events Index	X_0(nm)	Y_0(nm)	τ(s)	Accumulative Time (s)
1	-62.54	399.17	3.88	3.88
2	-303.9	435.67	2.36	6.24
3	151.38	786.63	9.305	15.545
4	211.51	770.89	2.91	18.455
5	126.17	814.6	0.035	18.49
6	-109.8	350.2	3.13	21.62
7	-268.9	504.21	2.485	24.105
8	-367.3	437	0.025	24.13
9	1502.4	6.35	4.32	28.45
10	179.05	932.72	1.325	29.775
11	248.81	930.1	5.9	35.675
12	141.46	800.88	21.275	56.95
13	645.46	-654.9	8.295	65.245
14	108.82	915.56	16.995	82.24
15	122.46	1102.7	0.265	82.505
16	9.36	1138.5	2.93	85.435
17	112.89	983.15	2.075	87.51
18	113.02	1146.5	2.32	89.83
19	-259	520.58	2.93	92.76
20	221.36	619.19	0.235	92.995

Events Index	X_0(nm)	Y_0(nm)	τ(s)	Accumulative Time (s)
1	-62.54	399.17	4.32	4.32
2	-303.9	435.67	0.025	4.345
3	151.38	786.63	2.36	6.705
4	211.51	770.89	9.305	16.01
5	126.17	814.6	0.235	16.245
6	-109.8	350.2	2.32	18.565
7	-268.9	504.21	2.91	21.475
8	-367.3	437	16.995	38.47
9	1502.4	6.35	3.88	42.35
10	179.05	932.72	8.295	50.645
11	248.81	930.1	2.93	53.575
12	141.46	800.88	5.9	59.475
13	645.46	-654.9	1.325	60.8
14	108.82	915.56	2.93	63.73
15	122.46	1102.7	0.035	63.765
16	9.36	1138.5	3.13	66.895
17	112.89	983.15	2.485	69.38
18	113.02	1146.5	21.275	90.655
19	-259	520.58	0.265	90.92
20	221.36	619.19	2.075	92.995

Supplementary Figure 8. Illustration of randomization of the individual catalytic events from a single Au nanorod catalyzing the deacetylation reaction. Each catalytic event has a microscopic reaction time τ, a spatial location (x, y), and a temporal sequence represented by its event index. (**a**) Randomization of the temporal sequence of the individual catalytic events. (**b**) Randomization of the spatial locations of individual catalytic events. (**c**) Randomization of both the temporal sequence and spatial locations of individual catalytic events.

After the above randomizations, we re-computed the intra- and inter-particle cross-correlation coefficients ρ_{τ_i,τ_j}. We use the experimental data from the Au nanorods in catalyzing the deacetylation reaction as illustrations here. For intraparticle catalytic communication, the characteristic exponential dependences of ρ_{τ_i,τ_j} on intraparticle Δx_{ij} and $\overline{\Delta t_{ij}}$ vanishes, and it stays essentially flat at the residual value of ~0.03 (Supplementary Figure 9a, b). Similarly, for interparticle catalytic communication, the dependences of ρ_{τ_i,τ_j} on interparticle Δx_{ij} and $\overline{\Delta t_{ij}}$ also vanishes (Supplementary Figure 9c, d); ρ_{τ_i,τ_j} here is flat and has a similar residual value of ~0.03. These residual values represent the spurious contribution to the cross-correlation coefficient, which is also present in simulations of random catalytic events (SI Section 8 below). *Therefore, the experimental observed Δx_{ij} and $\overline{\Delta t_{ij}}$ dependences of the cross-correlation coefficient ρ_{τ_i,τ_j} are inherently related to the temporal sequence and spatial locations of the individual catalytic events*.

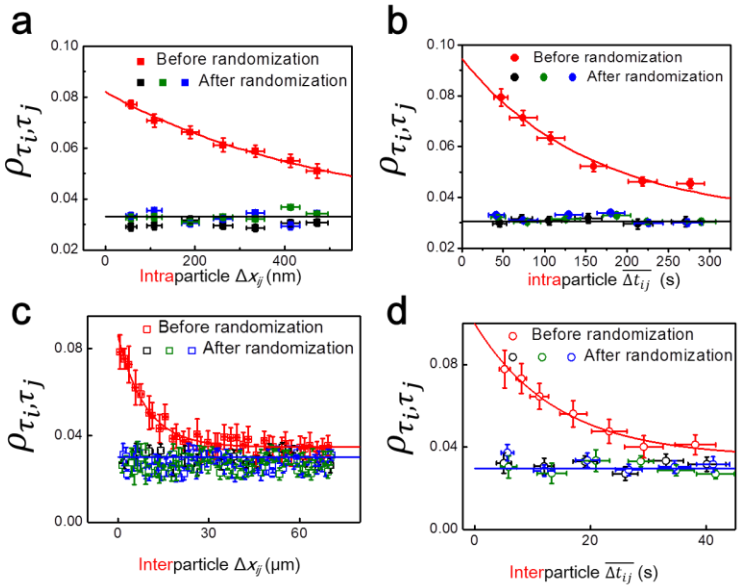

Supplementary Figure 9. Effect of catalytic event randomizations on the cross-correlation coefficient ρ_{τ_i,τ_j} for intra- and inter-particle catalytic communications, using as an example Au nanorods in catalyzing the deacetylation reaction. (**a, b**) ρ_{τ_i,τ_j} vs. intraparticle Δx_{ij} or $\overline{\Delta t_{ij}}$ before and after randomization. (**c, d**) ρ_{τ_i,τ_j} vs. interparticle Δx_{ij} or $\overline{\Delta t_{ij}}$ before and after event randomization. The black, green and blue points represent the temporal, spatial, or both randomizations, respectively. Red lines are all exponential fits. Black or blue lines are the mean values. x error bars are s.d. and y error bars are s.e.m.

8. Simulations show that temporally random catalytic events do not show intra- or inter-particle catalytic communications, but have a spurious residual cross correlation

As a further control, we performed simulations of catalytic events on single nanorods of various lengths, on which the catalytic events occur in a temporally random fashion, but the time-averaged turnover rate and the spatial distribution of catalytic events match those we experimentally measured, for example Au nanorods in catalyzing the deacetylation reaction[2]. Using the simulated events, we then evaluated whether or not these temporally random catalytic events *would* show intra- and inter-particle catalytic communications.

In the simulation, we used 200 nanorods, each modeled as a rectangle with length in the range of 200 to 600 nm (Supplementary Figure 10b) (i.e., ignoring the two ends that are pseudo-half-spheres), similar to the Au nanorod core length of those studied experimentally (Supplementary Figure 10a). The width of the nanorod core was fixed at 21 nm; this is about the actual average width of the nanorod core of $mSiO_2$-coated Au nanorods, which do not vary much from rod to rod[2]. The nanorods in the simulations were treated as 2-D objects, as our experimental imaging was in 2-D.

For each nanorod of length L in the simulation, its catalytic activity at a specific location along its length was taken from our previous study of Au nanorods in catalyzing the deacetylation reaction of amplex red[2]. In this previous study, we found that these nanorods have an activity gradient along their lengths, with their centers more active, and decaying linearly toward the two ends, attributable to an underlying defect density gradient that is the highest at the center and less toward the two ends. The local catalytic activity along the length of a single nanorod was found to follow the relationship:

$$k_L(x) = -2\beta_L x + k_{c,L} \tag{5}$$

where $k_L(x)$, in $s^{-1}\,nm^{-2}$, is the catalytic activity at a distance x from the center of a nanorod with length L. Parameter β_L, in $s^{-1}\,nm^{-3}$, is the activity gradient from the nanorod center toward the two ends. $k_{c,L}$, in $s^{-1}\,nm^{-2}$, is the activity at the center position. Both β_L and $k_{c,L}$ were found to be dependent on the nanorod length L. Using the experimental data from our previous study (Supplementary Figure 10c-d), for each nanorod with a length L, we determined its β_L and $k_{c,L}$, and thus $k_L(x)$, which was used as input parameters for our simulations.

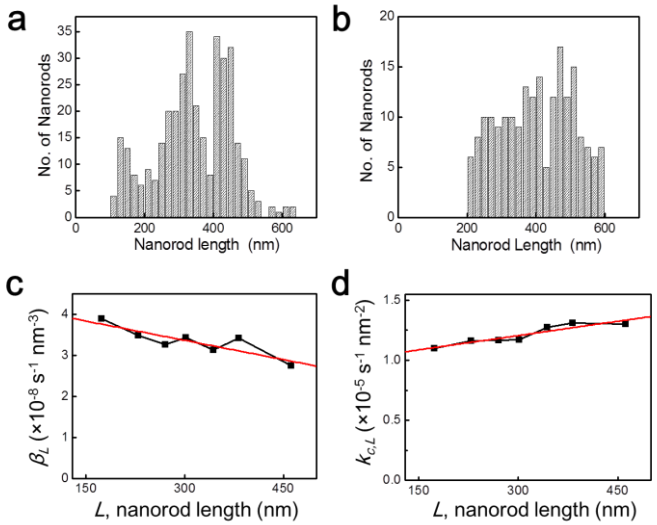

Supplementary Figure 10. (**a**) Length distribution of the as-synthesized Au nanorods from our previous study[2]. (**b**) Length distribution of the nanorods in simulations**.** (**c, d**) Dependence and linear fitting of β_L and $k_{c,L}$ on nanorod length L from Zhou et al[2]: (**c**) β_L (×10^{-8} s^{-1} nm^{-3}) = –0.00314 L (nm) + 4.314; (**d**) $k_{c,L}$ (× 10^{-5} s^{-1} nm^{-2}) = 0.00079L (nm) + 0.968.

In order to assign the spatial locations of the simulated catalytic events on the surface of nanorods, we divide every simulated nanorod into segments with 10 nm in length (a size smaller than the spatial resolution of ~40 nm in our experimental imaging of reaction locations). The local activity $k_L(x)$ (in $s^{-1}\,nm^{-2}$) of each segment for a nanorod of length L can then be determined from Supplementary Eq. (5) and data in Supplementary Figure 10c-d. Moreover, the Au surface area of each segment is ~660 nm^2, treating the nanorod as a cylinder with a diameter of 21 nm. Using $k_L(x)$ and the surface area of each segment, the reaction rate (in s^{-1}) of each segment can be obtained, giving rise to a volcano-shaped activity profile from the center toward the two ends (Supplementary Figure 11c). Based on this profile, the number of catalytic events is then sampled for each segment, until the total number of events of the whole nanorod reaches about 8000, which is approximately the number of events we observed experimentally for a single nanorod. Within each segment of 10 nm, the location along the nanorod long axis of each catalytic event is randomly assigned. Considering the real catalyst particles are core-shell

nanostructures with a mesoporous SiO_2 shell of ~80 nm in thickness, the positions of simulated events are randomly distributed in the direction perpendicular to the nanorod long axis (Supplementary Figure 11b). By doing so, we can simulate the 2-D spatial distribution of catalytic events on a single nanorod with length L (Supplementary Figure 11a).

We next determined the microscopic reaction time τ for each catalytic event in the simulation within the event sequence for the *whole* nanorod. For temporally random catalytic events in which the catalytic kinetics contains one rate-limiting step, the distribution of τ follows a single-exponential decay, where the exponential time constant is equal to $\langle\tau\rangle$. Here, $\langle\tau\rangle^{-1}$ is equivalent to the average reaction rate of the nanorod as whole, which can be obtained from the reaction rates of all segments described above. Therefore, the exponential distribution of τ can be determined for a nanorod of length L (Supplementary Figure 11d). All the catalytic events, whose spatial distribution on the nanorod was determined earlier, were then assigned a microscopic time τ by sampling the exponential distribution. Taken all together, the simulation produces a sequence of catalytic events that are temporally random (e.g., Supplementary Figure 11e), but spatially follow the distribution observed experimentally, and have a time-averaged rate consistent with experimental data.

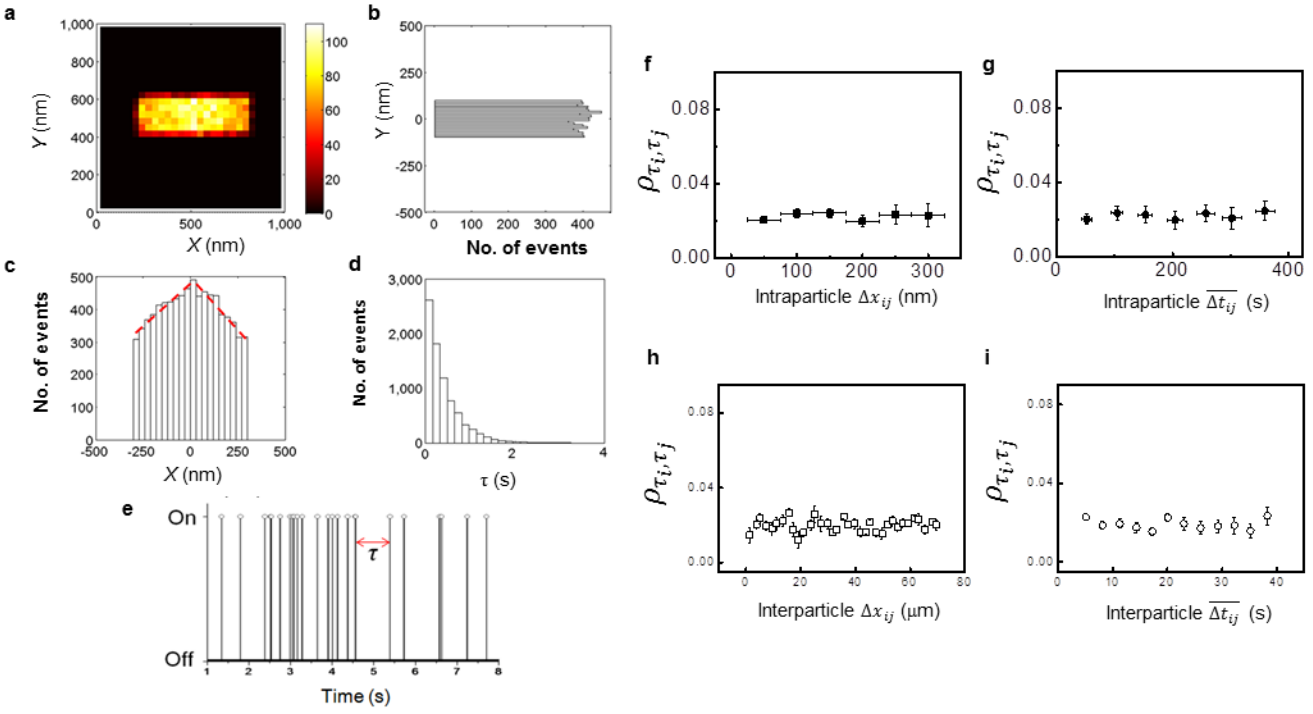

Supplementary Figure 11. Simulated temporally random catalytic events do not show intra- and inter-particle catalytic communication behaviors. (a-e) Exemplary simulated catalytic events on a single nanorod of length = 500 nm. (**a**) Two-dimensional spatial histogram of catalytic events in 20 × 20 nm^2 bins. The two hemisphere ends are omitted here, as we did not include in the analysis of experimental data either. (**b, c**) Spatial distributions of catalytic events perpendicular to (**b**) and along (**c**) the nanorod long axis. Red dash lines in **c** indicate the linear gradient of catalytic activity from the center toward the two ends along the nanorod length as described by Eq S(5. (**d**) Distribution of τ of the simulated catalytic events follows a single exponential distribution. (**e**) A segment of simulated time trajectory of event sequence for the whole nanorod. (**f-i**) Cross-correlation coefficient ρ_{τ_i,τ_j} for probing intra- and inter-particle catalytic communications obtained from simulations as those in a-e. (**f, g**) intraparticle ρ_{τ_i,τ_j} vs. the intraparticle distance separation Δx_{ij} or average time separation $\overline{\Delta t_{ij}}$. (**h, i**) Same as (**f, g**) but for interparticle ρ_{τ_i,τ_j}.

Using the simulated results of the 200 nanorods of various lengths, we performed the cross-correlation analysis to probe the existence of *intraparticle* catalytic communication, as we did on experimental results. To analyze potential *interparticle* catalytic communication using the simulated results, we needed to assign positions

to these 200 nanorods. Here we used the locations of nanorods on the quartz slide that we studied experimentally, and assigned these experimental locations randomly to the 200 simulated nanorods.

For the intraparticle analysis, Supplementary Figure 11f and g show ρ_{τ_i,τ_j} vs. the intraparticle distance separation Δx_{ij} and the average time separation $\overline{\Delta t_{ij}}$ between temporally subsequent catalytic events on different segments. No exponential decay behavior of ρ_{τ_i,τ_j} is observed with increasing Δx_{ij} or $\overline{\Delta t_{ij}}$, and ρ_{τ_i,τ_j} stays flat at a residual value of ~0.02, which represents a spurious contribution. Therefore, temporally random catalytic events do not show intraparticle catalytic communications.

Supplementary Figure 11h and i show the corresponding data for interparticle analysis. Again, ρ_{τ_i,τ_j} does not show any decay behavior with increasing interparticle distance separation Δx_{ij} and average time separation $\overline{\Delta t_{ij}}$ between temporally subsequent events on different nanorods, and it stays flat at ~0.02, which again represents a spurious contribution from random events to the cross-correlation coefficient. The independence of ρ_{τ_i,τ_j} on Δx_{ij} or $\overline{\Delta t_{ij}}$ here demonstrates that temporally random catalytic events do not show interparticle catalytic communications, either.

Altogether, the results from these simulations support that the intra- and inter-particle catalytic communications we observed experimentally are inherently related to the temporal relationship of the individual catalytic events, and that temporally random events do not possess similar properties.

9. Resorufin rebinding to nanocatalysts contributes to ~0.3% of the detected events and does *not* give rise to intra- or inter-particle catalytic communication behaviors

To ensure that the rebinding of the catalytic product resorufin to the nanocatalysts is not the cause for the observed intra- and inter-particle catalytic communications, we performed a control experiment where we followed in 5 nM resorufin into the microfluidic reactor and imaged resorufin binding to single nanocatalysts, using the $mSiO_2$-coated Au nanorods as a representative. Based on the background fluorescence level in the flow reactor, which is proportional to the concentration of resorufin in the solution, this 5 nM resorufin is about 10 times larger than the steady-state concentration of resorufin generated during the catalytic reaction under similar laser excitation and solution flow conditions. Supplementary Figure 12a shows that even under this 10× higher concentration of resorufin, the rate of detected events on a single Au nanorod is only ~3% of those detected during the Au nanorod catalyzed AR deacetylation and Rz deoxygenation reactions, *demonstrating that resorufin rebinding has no significant contribution (i.e., ~0.3%) to the detected events in catalysis*. The rate per Pd nanorod in the catalytic reaction is even larger due to the larger size of the particle. The average fluorescence on-time of individual resorufin in this rebinding control experiment is the same as those measured in the three catalytic reactions (~40 ms) (Supplementary Figure 12b), consistent with that the on-time is the adsorption of the product resorufin within the mesoporous of the $mSiO_2$ shell of the Pd/Au nanocatalysts, which should not differ when the resorufin is generated catalytically or rebound from the solution.

Using the detected resorufin rebinding events on single Au nanorods in this control experiment, we calculated the same cross-correlation coefficient ρ_{τ_i,τ_j} between temporally subsequent *adsorption* events that occur at different segments or at different nanorods. For both the intra- and inter-particle ρ_{τ_i,τ_j}, there are no trends of ρ_{τ_i,τ_j} being positive and decaying exponentially with increasing distance and average time separations between the temporally subsequent events (Supplementary Figure 12c-f). *Therefore, rebinding of resorufin to the nanocatalysts, even if it were to contribute to the detected events, does not give rise to the intra- and inter-particle communication behaviors.*

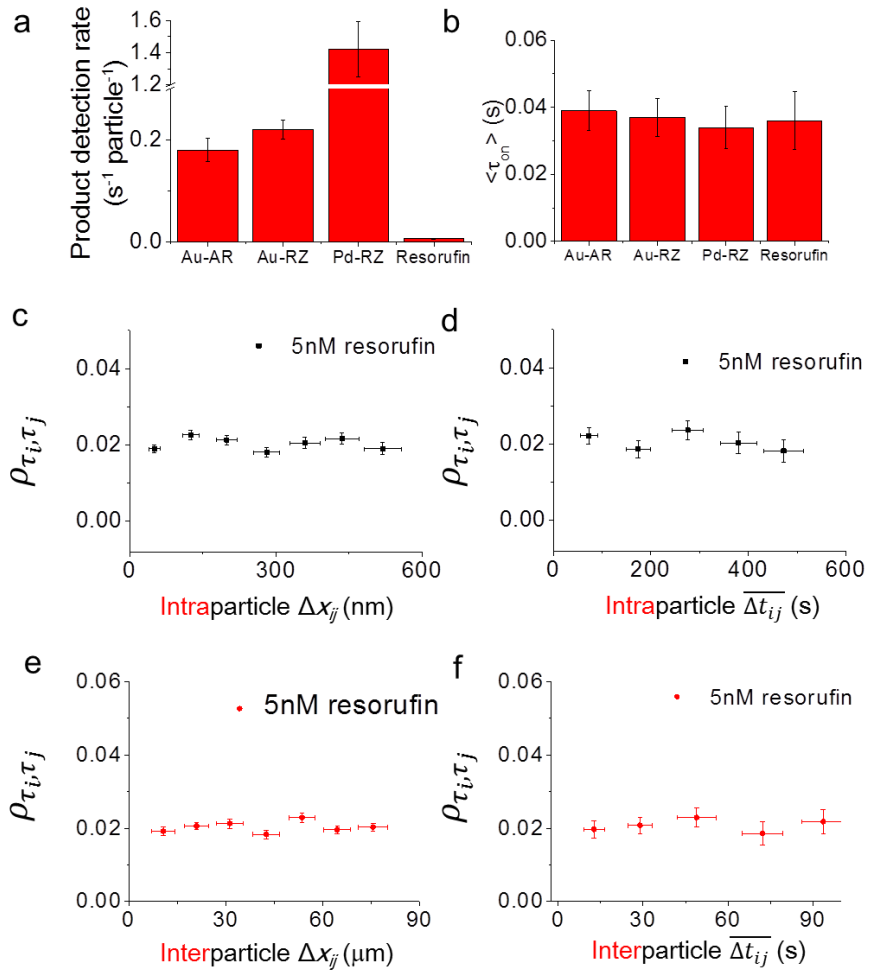

Supplementary Figure 12. (**a**) Average product detection rates in the Au-nanorod-catalyzed AR deacetylation reaction, Au-nanorod-catalyzed Rz deoxygenation reaction, Pd-nanorod-catalyzed Rz disproportionation reaction, and the resorufin rebinding at 5 nM on single Au nanorods. The data are averaged over 62, 56, 45, and 43 nanorods respectively. (**b**) The average fluorescence on-time in the four experiments as in **a**. (**c, d**) Pearson's cross-correlation coefficient $\rho_{\tau_i,\tau_j}(\Delta x_{ij}, \overline{\Delta t_{ij}})$ vs. the intraparticle distance separation Δx_{ij} or the average time separation $\overline{\Delta t_{ij}}$ of temporally subsequent adsorption events at two different segments on the same Au nanorod in the resorufin adsorption control experiment. (**e, f**) Same as **c**, **d**, but between adsorption events that occur on different nanorods.

10. Additional experimental results

10.1 Additional results on Pd nanorods in catalyzing Rz disproportionation

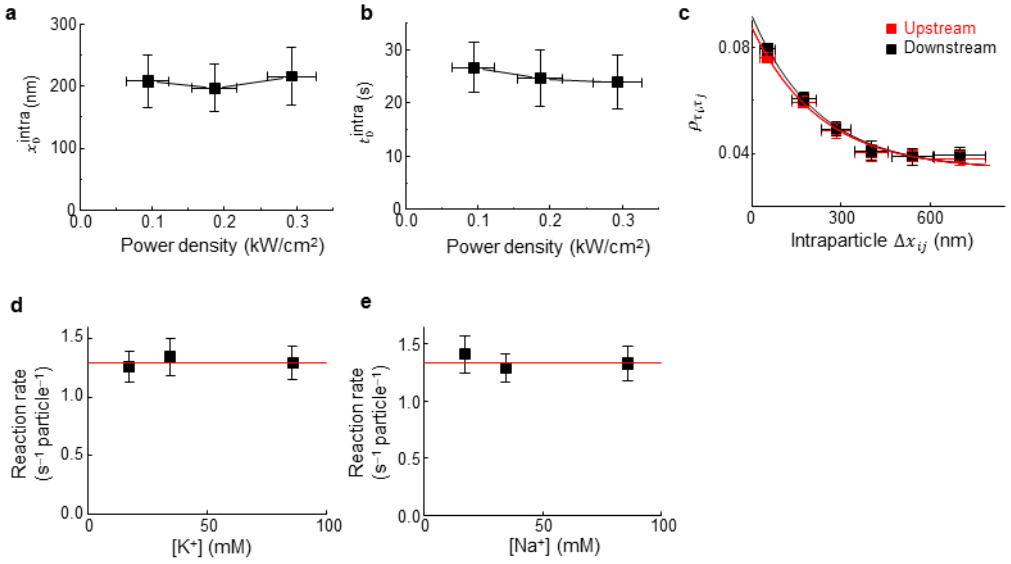

Supplementary Figure 13. Additional results on the *intra*particle catalytic communication within single Pd nanorods in catalyzing the photo-driven Rz disproportionation. (a-b) Laser power has no effect: x_0^{intra} (**a**) and t_0^{intra} (**b**) vs. the 532 nm laser excitation power density; no significant dependence is discernable. (**c**) **Solution flow has no effect:** Cross-correlation coefficient ρ_{τ_i,τ_j} vs. the intraparticle distance separation Δx_{ij} when the *i*-to-*j* intraparticle vector is pointed downstream (θ = 13±3°) or upstream (θ = 193±3°) along the solution flow at 180 μm s^{-1} flow rate. No significant differences are observed between the two curves. (**d, e**) **Spectator cations have no effect on Pd nanorod activity**. The averaged single-particle catalytic rate of Pd nanorods as a function of [K^+] and [Na^+] in the solution. The K^+ and Na^+ concentrations were varied by varying the buffer concentrations, in which they are the counter cations.

10.2 Additional results on Au nanorods in catalyzing AR deacetylation

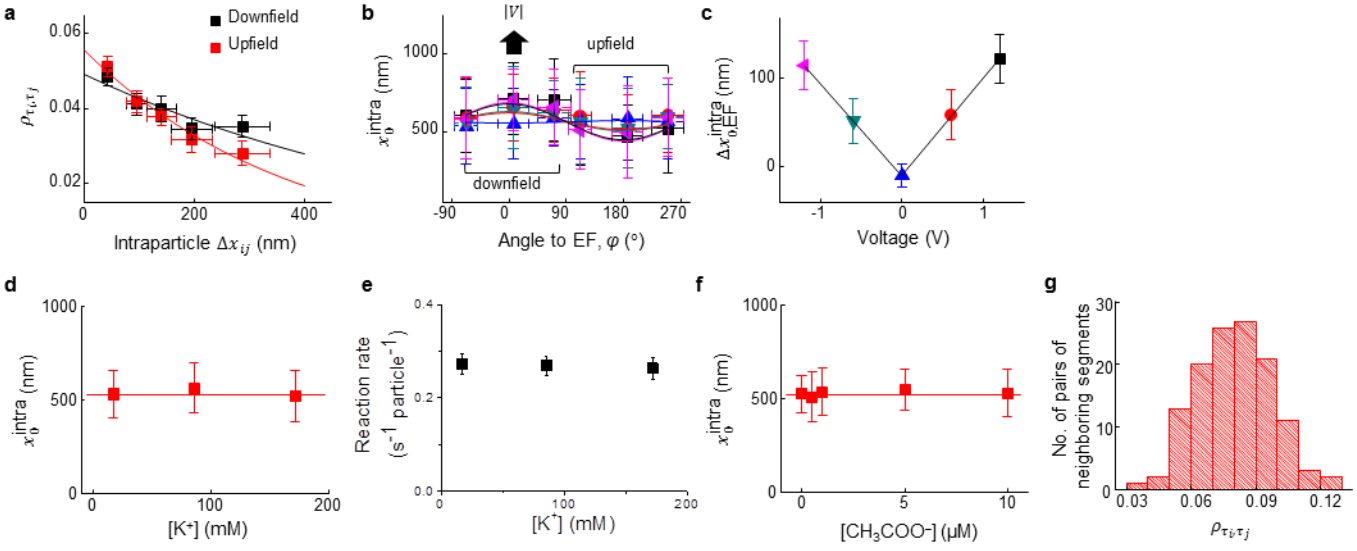

Supplementary Figure 14. Additional results on the *intra*particle catalytic communication of Au nanorods in catalyzing AR deacetylation. (a-c) EF effects indicate that the messenger for the intraparticle catalytic communication here is a positively-charged species: (**a**) ρ_{τ_i,τ_j} vs Δx_{ij} when the *i*-to-*j* intraparticle vector is pointed

downfield ($\varphi = 14 \pm 5°$) or upfield ($\varphi = 194 \pm 5°$) along the EF direction at 1.2 V. Lines: all exponential fits. (**b**) x_0^{intra} vs. orientation angle φ to the EF direction at various voltages. Lines: fits with cosine function (Supplementary Equation 1). (**c**) Cosine function amplitude $\Delta x_{0,\text{EF}}^{\text{intra}}$ vs. voltage from **c**. Symbols color-coded as in **c**; lines are eye-guides. (**d-e**) **Spectator cation does not affect the intraparticle catalytic communication or the reaction kinetics** (in this catalytic reaction, the only spectator cation is K^+, which comes from the phosphate buffer; the two reactants, amplex red and H_2O_2, were both obtained in their neutral forms**):** x_0^{intra} (**d**) vs. [K^+] in solution; no significant dependence is discernable. (**e**) The catalytic activities of single $mSiO_2$-coated Au nanorods are independent of [K^+] in the reaction solution. Data averaged over 46 nanorods. The [K^+] was varied by using a range of phosphate buffer concentrations (pH maintained at 7.2), in which the counter cation is K^+. (**f**) **The product acetate has no effect:** x_0^{intra} vs. externally added [CH_3COO^-]; no significant dependence is discernable. (**g**) An example of the distribution of the ρ_{τ_i,τ_j} values from individual pairs of neighboring segments of individual Au nanorods; the average here is 0.079 ± 0.006.

10.3 Results on *Au nanorods in catalyzing Rz deoxygenation*

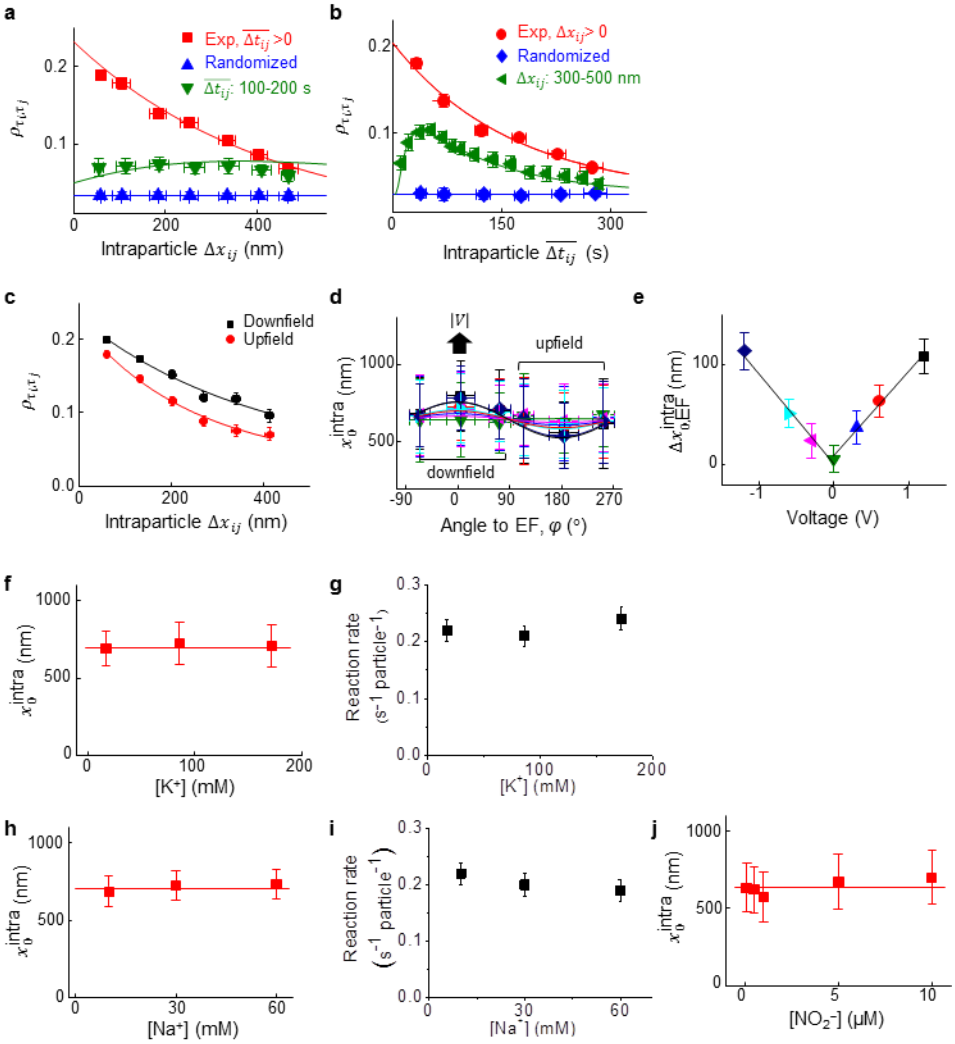

Supplementary Figure 15. Results on *intra*particle catalytic communication within single Au nanorods catalyzing Rz deoxygenation. (**a,b**) Pearson's cross-correlation coefficient ρ_{τ_i,τ_j} vs. the intraparticle distance separation Δx_{ij} or the average time separation $\overline{\Delta t_{ij}}$ of temporally subsequent reactions at different segments on the same nanorod (red), and after spatial (**a**) or temporal (**b**) randomization of the catalytic events (blue), and when $\overline{\Delta t_{ij}}$ or Δx_{ij} is constrained (green). *Note the cross-correlation amplitudes here are 0.213 ± 0.045 (**a**) and 0.183 ± 0.068 (**b**), significantly larger than that for the AR deacetylation reaction in Figure 1d-e, indicating that the strength of intraparticle catalytic communication can vary depending on the catalytic reaction*. Data averaged over >750 segments from >170 nanorods. Red lines: exponential fits

with distance constant x_0^{intra} = 624 ± 180 nm and time constant t_0^{intra} = 168 ± 36 s. Complete fitting parameters in Supplementary Table 2. Blue lines: horizontal fits. Green lines: fits with Supplementary Eqs. (16) and (22). *x* error bars are s.d. *y* error bars are s.e.m. (**c-e**) **EF effects indicate that the messenger for the intraparticle catalytic communication here is a positively-charged species:** (**c**) ρ_{τ_i,τ_j} vs Δx_{ij} when the *i*-to-*j* intraparticle vector is pointed downfield (φ = 15 ± 5°) or upfield (φ = 195 ± 5°) along the EF direction at 1.2 V. Lines: all exponential fits. (**d**) x_0^{intra} vs. orientation angle to the EF direction at various voltages, fitted with cosine function Supplementary Equation 1; (**e**) the cosine function amplitude $\Delta x_{0,\text{EF}}^{\text{inter}}$ vs. voltage from **d**. Symbols color-coded correspondingly. (**f-i**) **Spectator counter cations do not affect the intraparticle catalytic communication or the reaction kinetics (**in this catalytic reaction, the spectator cations are K^+, which comes from the phosphate buffer, and Na^+, which comes from the counter cation of the resazurin salt and NaOH that was used to neutralize $NH_2OH{\cdot}HCl$, a co-reactant): x_0^{intra} (**f** and **h**) vs. $[K^+]$ or $[Na^+]$ in the solution; no significant dependence is discernable. The $[K^+]$ concentration was varied by using a range of phosphate buffer concentrations (pH maintained at 7.2), in which the counter cation is K^+. The $[Na^+]$ was varied by using different concentrations of the co-reactant NH_2OH that was obtained commercially in the form of $NH_2OH{\cdot}HCl$ and neutralized by various amounts of NaOH. At this range of $[NH_2OH]$, the reaction kinetics is pseudo-zeroth order to $[NH_2OH]$[11,14]. (**g**,**i**) The catalytic activities of single Au nanorods are independent of $[K^+]$ or $[Na^+]$ in the reaction solution. Data averaged over 57 nanorods. (**j**) **The product nitrite has no effect:** x_0^{intra} vs. externally added $[NO_2^-]$; no significant dependence is discernable.

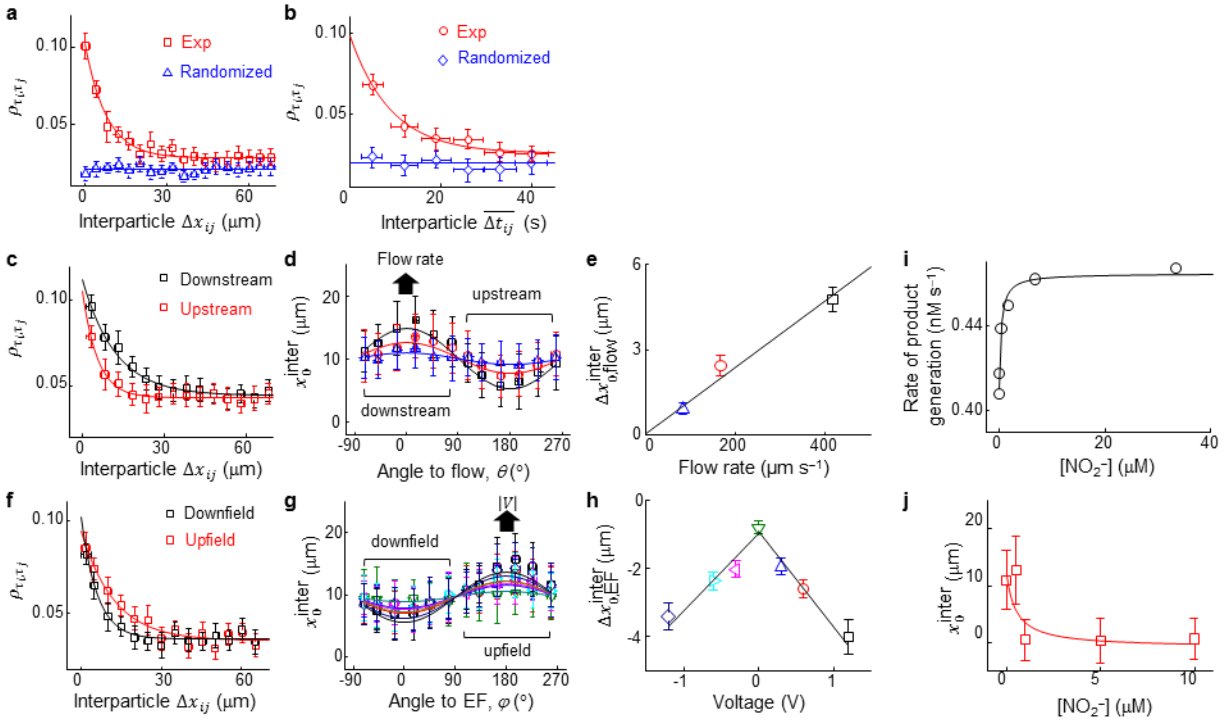

Supplementary Figure 16. Results on the *inter*particle catalytic communication between individual Au nanorods in catalyzing Rz deoxygenation. (**a**,**b**) Pearson's cross-correlation coefficient ρ_{τ_i,τ_j} vs. the interparticle distance separation Δx_{ij} or the average time separation $\overline{\Delta t_{ij}}$ of temporally subsequent reactions at two different nanocatalysts (red) and after spatiotemporal randomizations (blue). Data averaged over >170 nanocatalysts. Red lines: exponential fits with distance constant x_0^{inter} = 8.6 ± 2.2 μm and time constant t_0^{inter} = 7.7 ± 1.4 s, and offsets = 0.032. Blue lines: horizontal fits. (**c-h**) **Solution flow and EF effects show that the interparticle catalytic communication occurs via a molecular diffusion mechanism, involving a negatively-charged species:** (**c**, **f**) ρ_{τ_i,τ_j} vs. Δx_{ij} when the *i*-to-*j* interparticle vector is pointed downstream (θ = 15 ± 4°) or upstream (θ = 195 ± 4°) along the solution flow at 415 μm s^{-1} flow rate (**c**), or pointed downfield (φ = 14 ± 5°) or upfield (φ = 194 ± 5°) along the EF direction at 1.2 V (**f**). Lines: all exponential fits. (**d**,**g**) Dependences of the interparticle catalytic communication distance x_0^{inter} on the orientation angle relative to the flow direction at various flow rates (**d**) and to the EF direction at various voltages (**g**). Lines: fits with cosine function Supplementary Equation 1. (**e**,**h**) Cosine function amplitude $\Delta x_{0,\text{flow}}^{\text{inter}}$ vs. flow rate from **d**, and amplitude $\Delta x_{0,\text{EF}}^{\text{inter}}$ vs.

voltage from **g**. Symbols color-coded as in **d** and **g**. The negative voltages in **h** indicate flipping electrode bias. Lines: linear eye-guide. (**i,j**) **The reaction product NO_2^- is the interparticle catalytic messenger molecule:** (**i**) Initial product formation rate vs. [NO_2^-] in the solution at the ensemble level. Single-particle level data are in Supplementary Figure 27b. Line: fit with saturation function Supplementary Equation 2; $K_{1/2}$ = 0.46 ± 0.14 μM. (**j**) x_0^{inter} vs. [NO_2^-]. Line: fit with saturation function Supplementary Equation 3; $K_{1/2}$ = 0.53 ± 0.12 μM. X error bars in **a-d**, **f-g** are s.d. Y error bars in **a-c, f** are s.e.m., in **d-e, g-j** are s.d.

10.4 Results on Au nanoplates in catalyzing Rz deoxygenation

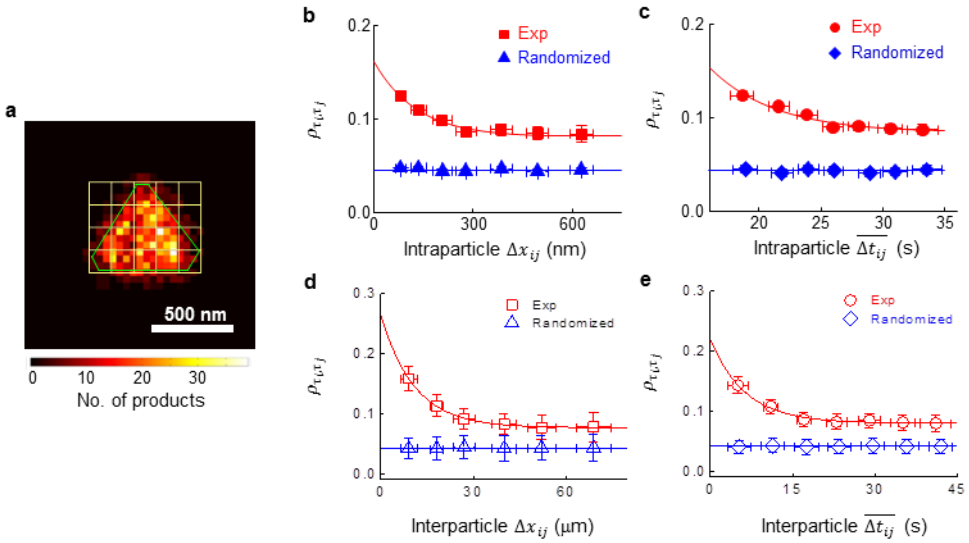

Supplementary Figure 17. *Intra*- and *inter*-particle catalytic communication of single Au nanoplates in catalyzing Rz deoxygenation. (**a**) Two-dimensional histogram of ~2350 fluorescent product molecules in 40×40 nm^2 bins from a single $mSiO_2$-coated Au nanoplate (Supplementary Figure 4j), mapped onto its SEM structural contour (green line; Supplementary Figure 4i). Yellow lines dissect the nanoplate into ~150×150 nm^2 square segments. Note the nanoplate has been rotated from that in Supplementary Figure 4i-j to have one edge being horizontal. (**b**, **c**) Pearson's cross-correlation coefficient ρ_{τ_i,τ_j} vs. the intraparticle distance separation Δx_{ij} or the average time separation $\overline{\Delta t_{ij}}$ of temporally subsequent reactions at different segments on the same nanoplate (red), and after spatial (**b**) or temporal (**c**) randomization of the catalytic events (blue). Data averaged over ~520 segments from ~50 nanoplates. Lines: exponential fits with distance constant x_0^{intra} = 130 ± 22 nm and time constant t_0^{intra} = 5.5 ± 0.6 s. Complete fitting parameters summarized in Supplementary Table 2. (**d, e**) Same as **b**-**c**, but for interparticle cases. Lines: exponential fits with distance constant x_0^{inter} = 11.5 ± 0.7 μm and time constant t_0^{inter} = 6.2 ± 0.6 s. X error bars are s.d. Y error bars are s.e.m.

10.5 The temporal memories t_0 of both intra- and inter-particle catalytic communications are unaffected by the solution flow, electric field, and presence of cations and anions in the solution: Au nanorods in AR deacetylation reaction as an example

No effect on the temporal memory of intraparticle catalytic communications. The temporal memories t_0^{intra} of intraparticle catalytic communications within single Pd and Au nanorods show no significant dependence on the nanorod's orientation to the solution flow direction or the EF direction (e.g., Supplementary Figure 18a-b). The independence on the solution flow is expected, as the catalytic reactions occur on the metal surface and the $mSiO_2$ shell would shield any influence from the solution flow on intraparticle processes. The independence on the EF is also consistent with our proposed hole migration mechanism, in which a surface localized hole is a catalytic messenger. In this mechanism, the temporal memory should correspond to the lifetime of this surface hole on the catalyst particle, which is likely not to be dependent on externally applied EF.

The independence of t_0^{intra} on externally added anions or cations is expected (e.g., Supplementary Figure 18c-d), as these anions and cations play no roles in intraparticle catalytic communication.

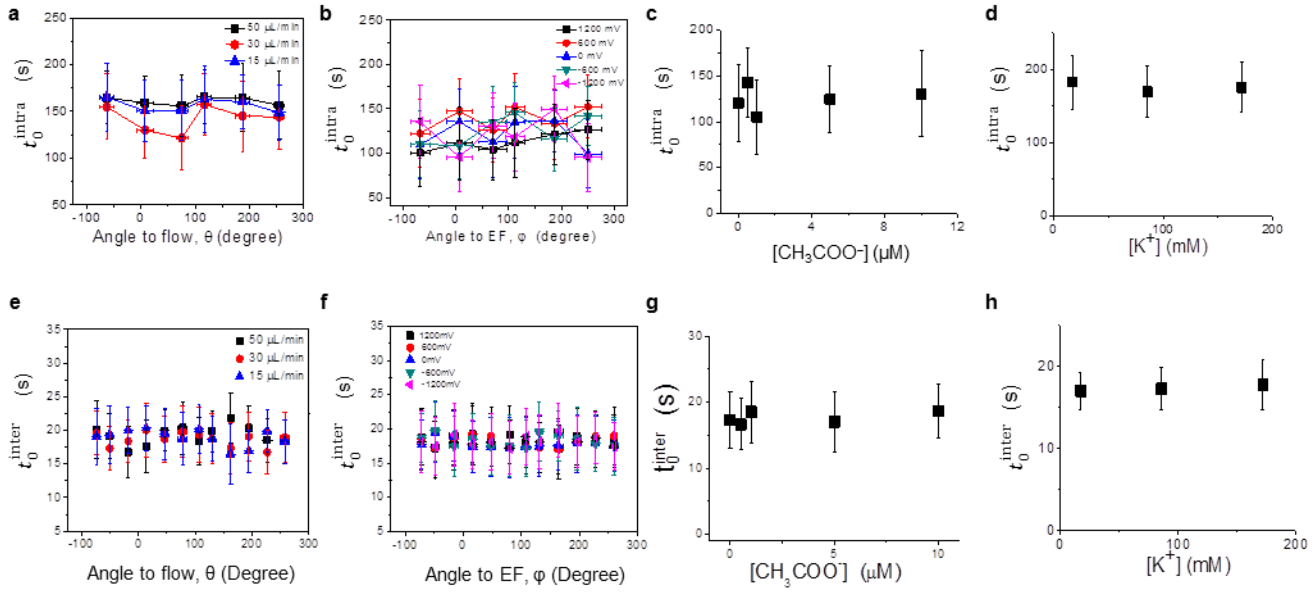

Supplementary Figure 18. The temporal memories of intraparticle (a-d) and interparticle (e-h) catalytic communication of Au nanorods in catalyzing AR deacetylation do not change significantly across a range of solution flow, electric field, product anion, and spectator cation conditions. Intra- and inter-particle catalytic communication temporal memory vs. the inter-nanorod orientation angle θ to the solution flow direction (**a**, **e**), the angle φ to the EF direction (**b, f**), externally added [CH_3COO^-] (**c, g**), and spectator cation [K^+] in the solution (**d**, **h**); no significant dependence is discernable in any case.

No effect on the temporal memory of <u>inter</u>particle catalytic communications because the messenger molecules spent <0.1% of its diffusing time in the solution. The temporal memories t_0^{inter} of interparticle catalytic communications between individual Au nanorods show no significant dependence on the inter-nanorod vector orientation to the solution flow direction or the EF direction or on the added anionic interparticle catalytic messenger (e.g., Supplementary Figure 18e-g), even though the mechanism here is the diffusion of negatively-charged product molecule (acetate or nitrite). Below we provide explanations of these independences.

Because of the molecular diffusion mechanism, the temporal memory t_0^{inter} of interparticle catalytic communication corresponds to the average time that takes for the messenger molecule (i.e., acetate or nitrite) to diffuse from the Au surface of a nanocatalyst to reach the Au surface of another nanocatalyst at a distance away. This distance corresponds to the interparticle catalytic communication distance x_0^{inter}, and it includes the distance in the solution (L_{solution}) and the distances in the $mSiO_2$ shell (L_{shell}) on both nanocatalysts through which the messenger molecule has to travel through via diffusion (Supplementary Figure 19):

$$x_0^{\text{inter}} = L_{\text{solution}} + 2L_{\text{shell}} \qquad (6)$$

L_{shell} = 85 nm, which is the average thickness of the $mSiO_2$ shell on the Au nanorods. For nanorods in catalyzing the AR deacetylation reaction, x_0^{inter} = 10.5 μm (Supplementary Table 2), and thus L_{solution} = 10.33 μm.

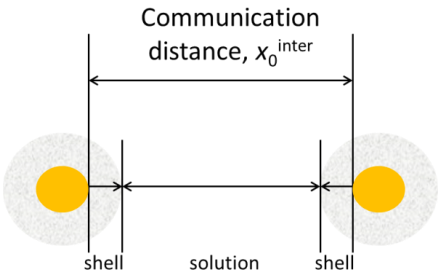

Supplementary Figure 19. Components of the interparticle catalytic communication distance, which includes the shell thickness on two Au nanocatalysts and the distance within the solution that the messenger molecule needs to travel through. The nanocatalysts are approximated here as spheres to omit the geometric anisotropy of nanorods.

Within each travel segment, the messenger molecule's travel distance should follow the 2-dimensional Brownian diffusion behavior, $L^2 = 4Dt$, where t is the time spent in each of the travel segment (note our imaging is 2-dimensional projection). And the total travel time corresponds to t_0^{inter} (=18.1 s, for nanorods in AR reaction; Supplementary Table 2), which includes both the time spent in the solution ($t_{solution}$) and that in each of the two shells (t_{shell}) on the two nanocatalysts:

$$t_0^{inter} = t_{solution} + 2t_{shell} \quad (7)$$

The diffusion coefficient of acetate in solution ($D_{solution}$) is 1.7×10^{-9} m^2 s^{-1}.[41] Therefore,

$$t_{solution} = \frac{(L_{solution})^2}{4D_{solution}} = 0.016 \text{ s} \quad (8)$$

$$t_{shell} = \frac{t_0^{inter} - t_{solution}}{2} = 9.09 \text{ s} \quad (9)$$

Therefore, the messenger molecule that diffuses to mediate interparticle catalytic communication only spends a <0.1% of its diffusing time in the solution (i.e., $t_{solution}/t_0^{inter}$ = (0.016 s)/(18.1 s) × 100% = 0.09%, < 0.1%), and >99.9% of its time is spent diffusing through the two $mSiO_2$ shells. It is thus not surprising that the solution flow and EF do not change the temporal memories of interparticle catalytic communication.

Similarly, the independence of t_0^{inter} on the externally added [acetate] or [nitrite] is expected, as the major component of t_0^{inter} is the diffusion time within the $mSiO_2$ shell of the interparticle catalytic messenger (i.e., acetate or nitrite), not that in the solution. The independence on the added cation is expected (Supplementary Figure 18h), as the cations do not play a role in interparticle catalytic communications.

11. The intraparticle catalytic communication distance x_0^{intra} and temporal memory t_0^{intra} are independent of experimental time resolution, segment size, catalytic activity, and fluorescence intensity threshold

Here we present controls regarding our data analysis procedures, using as examples the data from Au nanorods in catalyzing the deacetylation reaction.

11.1 They are independent of experimental time resolution within experimental error

Here we binned every two consecutive frames in the original fluorescence movie so that the image exposure time increased by a factor of two (i.e., time resolution decreased by 2 times) and analyzed the subsequent results. The results are summarized in Supplementary Figure 20 below.

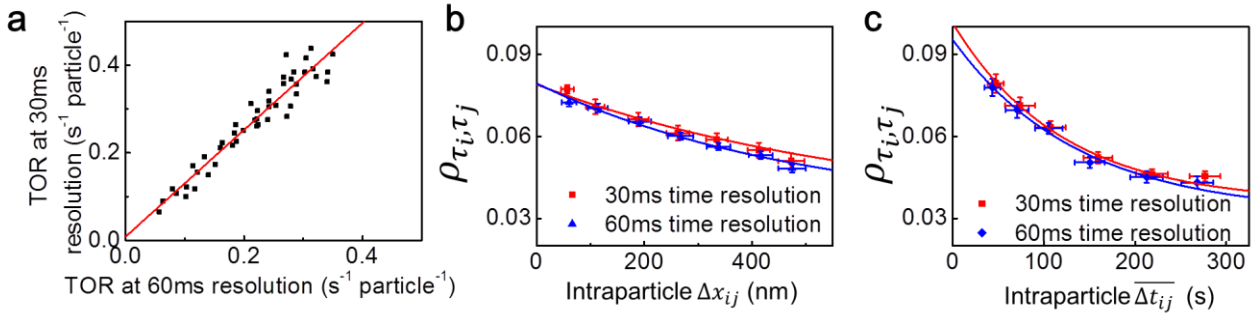

Supplementary Figure 20. Examination of intraparticle catalytic communication vs. experimental time resolution for Au nanorods in catalyzing the AR deacetylation. (**a**) Correlation of measured single-particle turnover rate at 30 ms and 60 ms time resolution. Each dot is for one nanorod. The line is a linear fit with the slope of 1.22 ± 0.05, bigger than one, indicating that at lower time resolution (i.e., 60 ms) the observed turnover rate for each nanorod is lower. This slower apparent turnover rate is expected, because the decrease in time resolution will lead to missing detection of some of the faster (i.e., shorter fluorescence on-time) catalytic events. (**b,c**) Dependence of the intraparticle cross-correlation coefficient ρ_{τ_i,τ_j} on the intraparticle distance separation Δx_{ij} (**b**) or average time separation $\overline{\Delta t_{ij}}$ (**c**) at the two different time resolutions. Exponential fits (lines) in **b** give the intraparticle catalytic communication distance x_0^{intra} of 518 ± 160 nm at 30 ms time resolution and 502 ± 148 nm at 60 ms time resolution, within error bars of each other; residual correlation offset at 0.032 ± 0.005. Exponential fits in **c** give the intraparticle catalytic communication temporal memory t_0^{intra} of 128 ± 32 s at 30 ms time resolution and 137 ± 26 s at 60 ms time resolution, also within error bars of each other; residual correlation offset at 0.034 ± 0.009. Y error bars in **b** and **c** are s.e.m. X error bars in **b** and **c** are s.d. **Therefore, the intraparticle catalytic communication distance x_0^{intra} and its temporal memory t_0^{intra} are independent of the experimental time resolution.** Note that practically, the time resolution cannot be too slow to dis-allow sufficient detection of catalytic events; otherwise, the imaging experiments would not be possible.

11.2 They are independent of the segment length in dissecting the individual nanorods

We examined the dependences of the intraparticle communication distance x_0^{intra} and temporal memory t_0^{intra} on the segment length. As our spatial resolution is about ~40 nm,[42] making the segment shorter than 40 nm is meaningless. On the other hand, if the length of segments is too long, very few segments could be obtained on a single nanorod that has a limited length of up to ~700 nm. Therefore, we varied the segment length from 38 nm to 95 nm (Supplementary Figure 21).

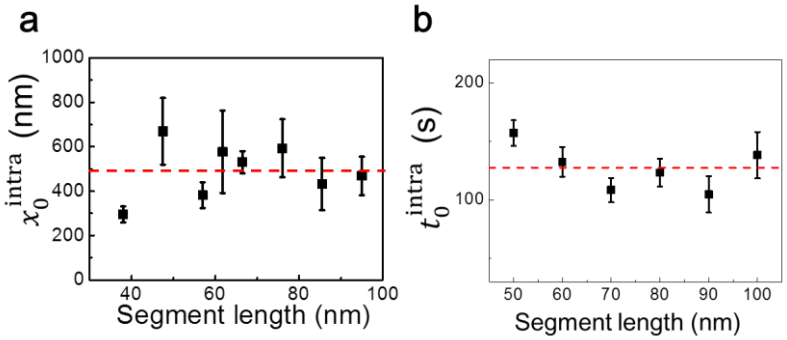

Supplementary Figure 21. Intraparticle catalytic communication distance x_0^{intra} (**a**) and temporal memory t_0^{intra} (**b**) vs. the segment length for Au nanorods in catalyzing the deacetylation of AR. **Both x_0^{intra} and t_0^{intra} are essentially independent of the segment length.** The dash lines mark the overall averages. The *y*-error bars are s.d.

11.3 They are independent of the nanorod's catalytic activity

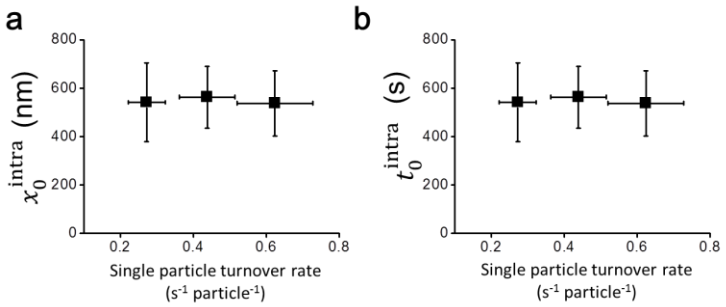

Supplementary Figure 22. Intraparticle catalytic communication distance x_0^{intra} (**a**) and temporal memory t_0^{intra} (**b**) vs. single-particle turnover rate (i.e., activity) for Au nanorods in catalyzing the deacetylation of AR. Within each batch of sample, individual nanorods show natural heterogeneity in catalytic activity, allowing us to sort them into three groups of different catalytic activity, analyzing them in each group to determine the dependence on the single-nanorod activity. **Both x_0^{intra} and t_0^{intra} are essentially independent of the nanorod's catalytic activity.** The *x*,*y* error bars are s.d.

11.4 They are independent of the fluorescence intensity threshold for selecting catalytic events on each nanocatalyst

In analyzing the original fluorescence movies of catalytic product formations, we automated the selection of the fluorescence burst signals by initially thresholding the fluorescence intensity vs time trajectory from a single nanocatalyst (see data analysis procedures in Section 4). The value of the threshold was optimized by comparing the data from a nanocatalyst under catalysis with those from a sample area that has no catalyst (i.e., fluorescence background trajectory). The value of the threshold (4.5σ) was also set in the units of the standard deviation σ of the fluorescence background trajectory. After thresholding, the corresponding images of the selected fluorescence bursts were further analyzed by point-spread-function fitting, in which we obtained the fluorescence spot size, location, and integrated photon counts that could be further used to differentiate true fluorescence signals of single molecules from random background noises.

To probe if this initial fluorescence intensity threshold affects the intraparticle catalytic communication behavior, we analyzed the same experimental data while varying the threshold from 3σ to 5σ, again using the Au nanorods catalyzed AR deacetylation reaction as an example (Supplementary Figure 23).

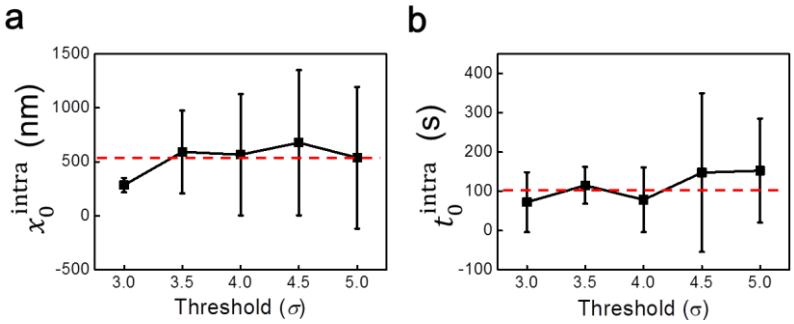

Supplementary Figure 23. Intraparticle catalytic communication distance x_0^{intra} (**a**) and temporal memory t_0^{intra} (**b**) vs the fluorescence intensity threshold. The dash lines represent the average values, which are 532 ± 148 nm and 113 ± 37 s, respectively. The y-error bars are s.d. **These results show that the intraparticle catalytic communication distance x_0^{intra} and temporal memory t_0^{intra} have no clear dependence on this fluorescence intensity threshold.** It is worth noting that with increasing threshold value, the number of selected fluorescence bursts decreased, giving lower apparent turnover rate for each nanocatalyst; this is expected, however, as higher threshold value would miss events that have relatively lower fluorescence intensities.

12. Both intraparticle and interparticle catalytic communications are independent of the laser light power density, supporting that laser excitation and thus surface plasmon resonance of Au play insignificant roles

The Au nanorods and nanoplates are both plasmonic particles, and their localized surface plasmon resonances (LSPR)[9,43-49] overlap with the wavelength of the laser (532 nm) that we used to induce the fluorescence of the catalytic product resorufin. To probe whether LSPR excitation would play any role in the observed intraparticle and interparticle catalytic communications, we examined their dependence on the power density of the laser light, using Au nanorods as the representative system.

In our experiments, the 532 laser beam was used to illuminate a ~50×100 μm^2 area via TIR geometry. Because of the Gaussian laser beam shape, there was a natural dispersion of the light power density across the illumination area: highest at the center and lower toward the periphery. And the local light power density at any location could be easily obtained from the laser illumination spatial profile and the total laser power illuminating the sample. As a result, individual Au nanorods experience different laser power density depending on their locations within the illumination area. We thus sorted individual Au nanorods into groups of similar local light power densities. As a control, we first examined whether their catalytic activity, normalized by their length, would depend on the light power density using the sorted individual nanorods. For both the deacetylation reaction and the deoxygenation reaction, the catalytic activities (i.e., reaction rates) of individual nanorods are essentially independent of local light power density within experimental error (Supplementary Figure 24a, f). *This independence indicates that within our experimental laser power density range (~0.05 to 0.4 kW/cm^2), the laser excitation, and thus LSPR excitation, has insignificant contributions to the observed catalytic reactions, consistent with our previous findings*[50] .

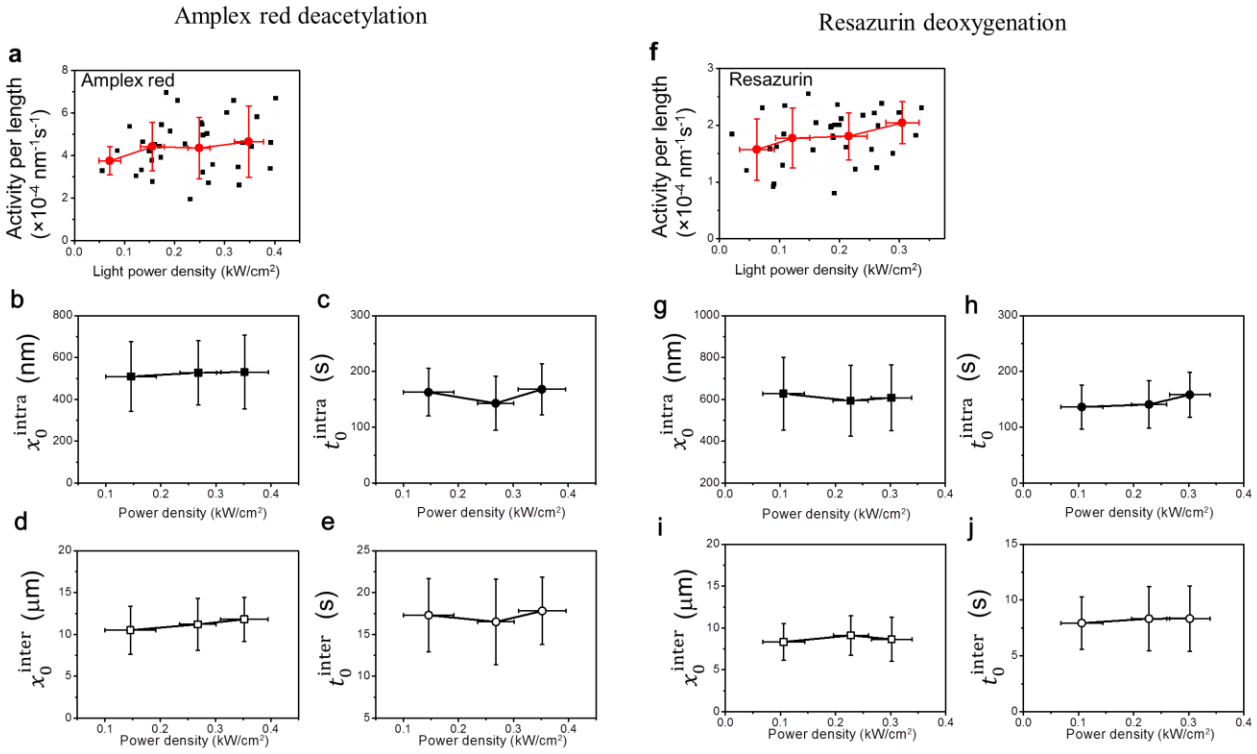

Supplementary Figure 24. Both intraparticle and interparticle catalytic communications of Au nanorods are independent of the laser light power density, supporting that laser excitation and thus surface plasmon resonance of Au play insignificant roles. (**a**, **f**) Catalytic activity of individual Au nanorods, normalized by the nanorod length, vs. the local 532 nm light power density in catalyzing the AR deacetylation (**a**) and Rz deoxygenation (**f**). Each black square represents a single nanorod; the red squares are average values after sorting the nanorods into groups of similar local light power density. Error bars are s.e.m. **(b-e, g-j)** Intraparticle and interparticle catalytic communication distance x_0 and

temporal memory time t_0 of Au nanorods vs. the local 532 nm light power density in catalyzing the AR deacetylation reaction (**b-e**) and the Rz deoxygenation reaction (**g-j**).

We then examined the intraparticle and interparticle catalytic communications within each group of individual Au nanorods of similar light power density, and determined their catalytic communication distance x_0 and the temporal memory t_0. For both the deacetylation reaction and the deoxygenation reaction and for both intraparticle and interparticle catalytic communications, the determined x_0 and t_0 show no significant dependences on the local light power density (Supplementary Figure 24b-e and g-j). *These independences indicate that the laser light plays no significant roles in the observed catalytic communications; they also support that LSPR, which could be excited by the laser light, does not play any significant roles, either*.

13. Applying voltage across the reactor cell using two Cu or Pt electrodes results in a steady-state electrical current, and they also cause similar changes in intra- and interparticle catalytic communication distances

We used a two-electrode configuration potentiostat to apply a voltage ranging from −1.2 to 1.2 V across the microfluidic reactor of 5-8 mm in width in the *xy* imaging plane perpendicular to the solution flow direction (Supplementary Figure 3c). The electrodes (made of copper foil or platinum wire) were connected to the working and counter electrodes of the potentiostat. Here the voltage direction being orthogonal to the solution flow minimized the cross-influence between the electric field effect and the solution flow effect.

Upon applying the voltage using Cu electrodes, an electrical current can be detected, and it reaches a steady state after ~800 seconds (Supplementary Figure 25a). The steady-state current increases when the voltage magnitude increases, and the current changes direction when the voltage bias is flipped (Supplementary Figure 25a-b). This steady-state electrical current has contributions from both the charging current and some redox processes on the electrode. The charging current comes from the fact that the microfluidic reactor is under a continuous flow of the reactant solution, containing >100 mM electrolytes (e.g., phosphate buffer), giving its nonequilibrium state, and is indicated by that the steady-state current increases with increasing solution flow rate (Supplementary Figure 25c). The redox contribution is indicated by color changes of the Cu electrodes over a period of time (i.e., Cu electrode is likely oxidized) and visible formation of gas bubbles (possibly H_2 and O_2 formation from water electrolysis).

Using two Pt electrodes, similar behaviors were observed, although the steady-state electrical currents are smaller than those from Cu electrodes at the same voltages (Supplementary Figure 25d-e). The smaller currents here are likely due to much less redox contribution to the current, as Pt electrodes are inert and we did not observe visually significant formations of gas bubbles. The cosine function amplitudes $\Delta x_{0,\mathrm{EF}}^{\mathrm{intra}}$ using Pt electrodes are smaller (Supplementary Figure 25f-g), likely due to a smaller steady-state electrical current.

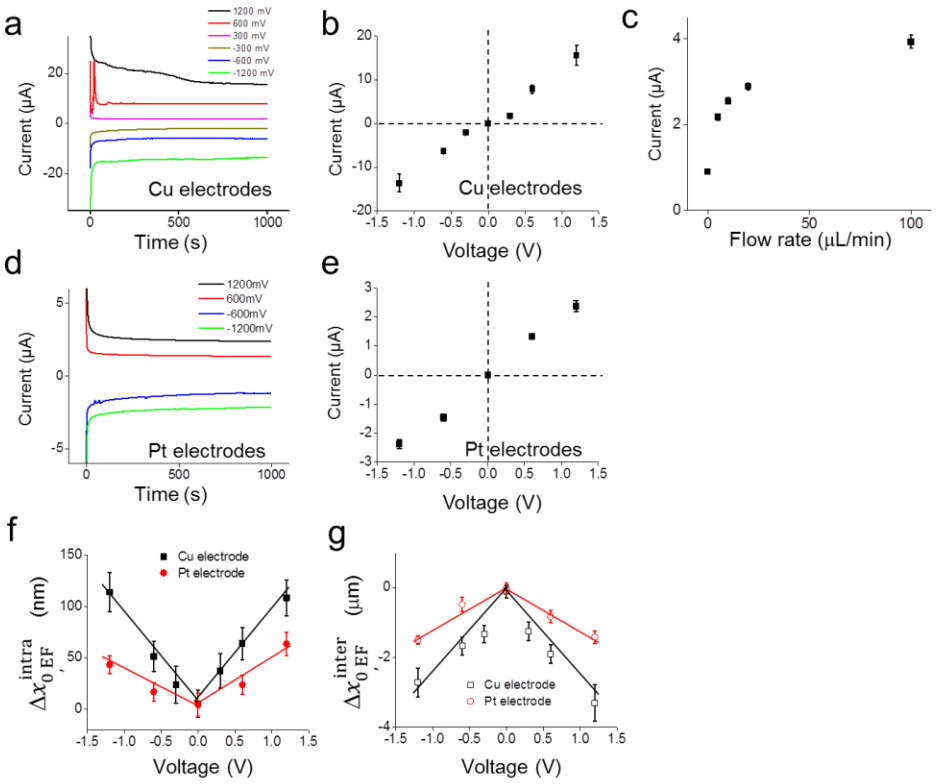

Supplementary Figure 25. (**a-e**) **Applying voltage using two metal electrodes results in a steady-state electrical current across the microfluidic reactor cell:** (**a**) Electrical current vs. time upon applying voltages at t = 0 using two Cu electrodes at a flow rate = 10 μL/min. (**b**) The steady-state current vs. applied voltage from **a**. (**c**) The steady-state current using two Cu electrodes vs. solution flow rate at a voltage of 0.3 V. (**d-e**) Same as **a** and **b** but using two Pt electrodes. (**f-g**) **Using Cu or Pt electrodes results in similar changes in intra- and inter-particle catalytic communication distances** (e.g., for Au-nanorod-catalyzed Rz deoxygenation): Cosine function amplitude $\Delta x_{0,\mathrm{EF}}^{\mathrm{intra}}$ vs. voltage from voltage manipulations of intra- (**f**) and inter-particle (**g**) catalytic communication distance of Au nanorods in catalyzing Rz deoxygenation, using Cu or Pt electrodes. Lines: all linear eye-guide. The data using Cu electrodes are the same as presented in Supplementary Figure 15e and Supplementary Figure 16h.

14. Acetate and nitrite promote the reaction rates of Au-particle-catalyzed AR deacetylation and Rz deoxygenation, respectively, whereas resorufin does not

14.1 Ensemble reaction kinetics shows that the reaction product acetate and nitrite can promote the Au-particle-catalyzed reaction rates of AR deacetylation and Rz deoxygenation, respectively, whereas the product resorufin does not

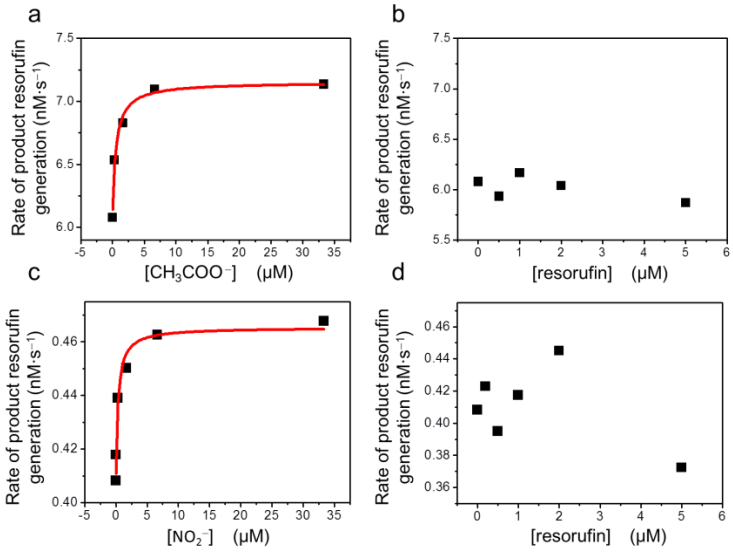

Supplementary Figure 26. Dependence of initial catalytic reaction rates on the presence of externally added reaction products measured at the ensemble level. 5 nm Au particles (PELCO® NanoXact™) were used as representative Au nanocatalysts here because of their size homogeneity compared with Au nanorod and nanoplate samples, which are heterogeneous and contain many different shapes of particles (Supplementary Figure 1f-i). (**a, b**) Initial rate of resorufin generation in AR deacetylation as a function of initial acetate (**a**) or resorufin (**b**) concentration in the solution. **The data show that acetate can promote the rate of Au-particle-catalyzed AR deacetylation — with increasing acetate concentration, the initial reaction rate increases and eventually saturates — whereas resorufin cannot, as its presence does not affect the initial reaction rate.** Reaction condition: 3 μM amplex red, 100 mM H_2O_2, 50 nM 5 nm Au nanoparticles, and variable potassium acetate or resorufin in 100 mM pH 7.1 phosphate buffer. Panel **a** is also presented as Fig. 5g in the main text. (**c, d**) Initial rate of resorufin generation in Rz deoxygenation as a function of initial nitrite (**c**) or resorufin (**d**) concentration in the solution. **The data show that nitrite can promote the rate of Au-particle-catalyzed Rz deoxygenation, whereas resorufin cannot.** Reaction condition: 20 μM resazurin, 10 mM NH_2OH, 200 nM Au nanoparticles, and variable nitrite or resorufin in 100 mM pH 7.1 phosphate buffer. Panel **c** is also presented as Supplementary Figure 16i. Red lines in **a** and **c** are fits with saturation rate Supplementary Equation (2), where $K_{1/2}$ is the half-saturation concentration of the promoter. For acetate, $K_{1/2}$ = 0.95±0.15 μM; for nitrite, $K_{1/2}$ is 0.46±0.14 μM. The apparent promoting effects of acetate and nitrite on the respective reactions are not strong, as the catalytic reaction rates only increase by up to 20%. It remains to be determined how mechanistically acetate or nitrite can have apparent promoting effects on the catalytic rate on the Au particle surfaces. One possibility is that acetate or nitrite can adsorb near the surface active sites, forming some interactions with the surface adsorbed reactant molecules and thus stabilizing the transition state, leading to catalytic rate enhancement. Other mechanisms may operate as well.

14.2 Single-particle catalytic kinetics of Au nanorods also shows that acetate and nitrite can promote the catalytic rates of AR deacetylation and Rz deoxygenation, respectively

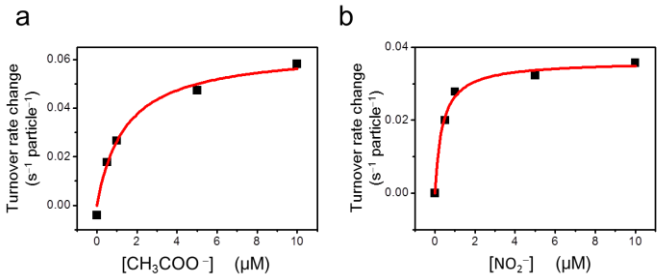

Supplementary Figure 27. Changes of single-particle catalytic turnover rate on the presence of externally added acetate in the AR deacetylation reaction (a) or the presence of added nitrite in the Rz deoxygenation reaction (b) catalyzed by mSiO$_2$-coated Au nanorods measured through single-molecule fluorescence imaging. The data are averaged over > 40 nanorods, which were monitored over several hours while the acetate or nitrite concentrations were increased step-wise. During the experimental time, the catalysts also deactivated appreciably; this deactivation effect over time was corrected for by using pre-determined deactivation rates, which were measured by monitoring the time-dependent catalytic activity of individual particles without changing reaction condition. AR reaction condition: 0.2 μM AR, 60 mM H_2O_2, and various acetate concentrations, in 100 mM pH 7.1 phosphate buffer. Rz reaction condition: 0.2 μM Rz, 10 mM NH_2OH, various concentrations of NO_2^-, in 100 mM pH 7.1 phosphate buffer. Red lines are fits with the saturation Supplementary Equation 2, with $K_{1/2}$ (acetate) = 1.1 ± 0.3 μM; $K_{1/2}$ (nitrite) = 0.47 ± 0.09 μM. **The results further support that acetate and nitrite can act as promoters of the respective surface catalytic reactions on the Au nanorods, because the single-molecule fluorescence imaging specifically detect reaction products on individual nanorods.**

15. Other possible mechanisms of intraparticle catalytic communication and the many rationales against them

15.1 Reaction heat dissipation should not be the mechanism

Another potential mechanism for intraparticle catalytic communication is the dissipation of heat generated in the catalytic reactions. But this mechanism would not involve the movement of charged species, and thus should *not* be the operating mechanism. We here discuss additional arguments against this possibility.

In this mechanism, the reaction heat could dissipate from one site to affect reactions at surrounding sites. From standard formation enthalpies, both the deacetylation of amplex red and the deoxygenation of resazurin are estimated to be exothermic reactions ($\Delta_r H°$ = –471.6 kJ mol^{-1} and –399.8 kJ mol^{-1}, respectively; see below for the details for the estimations; since we do not know for sure all the reaction products of the disproportionation reaction, we do not treat it here).

To probe if this heat dissipation could be relevant, we simulated the spatial and temporal profile of temperature on a nanorod using the 1-D thermal diffusion equation[51]:

$$\frac{\partial T}{\partial t} = \alpha \frac{\partial^2 T}{\partial x^2} = \frac{k}{\rho c_p} \frac{\partial^2 T}{\partial x^2} \qquad (10)$$

where α is the thermal diffusivity of the material, k is its thermal conductivity, ρ is its density, and c_p is its specific heat (Supplementary Table 1). Just for illustration, we assumed that a single reaction at one site would cause a local temperature jump (ΔT) of 5 K in a 100-nm-long segment on a 20-nm-diameter nanorod. The minimum energy (ΔE) needed to cause such a temperature jump is:

$$\Delta E = c_p \rho V \Delta T \qquad (11)$$

where V is the volume of the material the heat is released on. For a 20-nm diameter 100-nm long cylinder made of gold, ΔE would be about 3.9 × 10^{-16} J, which is equivalent to the amount of heat released for about ~820 $H_2(g)$

molecules to react with $O_2(g)$ to form $H_2O(l)$, a highly exothermic reaction ($\Delta H°$ is −286 kJ mol^{-1} for the reaction $H_2(g) + {}^1/_2O_2(g) = H_2O(l)$)[41]. This amount of heat is clearly much higher than that is possibly released from a single reaction of deacetylation of amplex red or deoxygenation of resazurin studied here. Therefore, a 5 K temperature jump represents a highly over-estimated case.

Using the thermal diffusion equation (Supplementary Equation (10)), we simulated the time-dependent temperature profile along one dimension (i.e., along the long axis of a nanorod) after a local 5 K temperature jump above room temperature (293 K). With thermal parameters for gold (Supplementary Table 1), the simulation shows that within about 1 ns, the initial temperature gradient from the local temperature jump is already dissipated, i.e., no significant temperature gradient is present along the length of nanorod (Supplementary Figure 28a). As our Au nanorods are coated with mesoporous silica and our experiments were done in an aqueous solution, we further did simulations using the thermal parameters for silica and water. The simulations show that for both these cases, the initial temperature gradient disappears in a time scale shorter than 1 μs because of heat dissipation (Supplementary Figure 28b and c). These timescales for heat dissipation are orders of magnitude faster than the temporal memory (10^1 to 10^2 of seconds) of the intraparticle catalytic communications of Au nanorods and nanoplates. We thus further conclude that reaction heat dissipation is likely not the reason for the long-range intraparticle catalytic communication within single Au nanocatalysts.

Supplementary Table 1. Parameters for Heat Dissipation Simulations (all from reference[41])

Materials	Thermal Conductivity k (W m^{-1} K^{-1})	Density ρ (kg m^{-3})	Specific Heat c_p (J kg^{-1} K^{-1})
Water	0.58	1000	4.18×10^3
Silica	1.3	2648	703
Gold	310	19.30×10^3	0.129×10^3

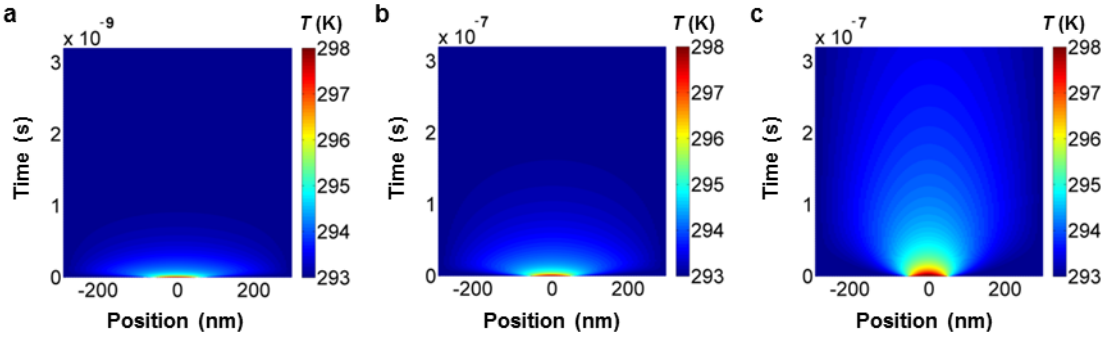

Supplementary Figure 28. Simulations of time-dependent 1-dimensional temperature profile after a local 5 K temperature jump at position 0, using thermal parameters for (**a**) gold, (**b**) silica, and (**c**) water. Parameters are listed in Supplementary Table 1.

Estimation of standard reaction enthalpies. We used the standard formation enthalpies to estimate the reaction enthalpies for the deacetylation reaction of AR and the deoxygenation reaction of Rz, according to the following balanced chemical equations (see also Figure 1b in the main text):

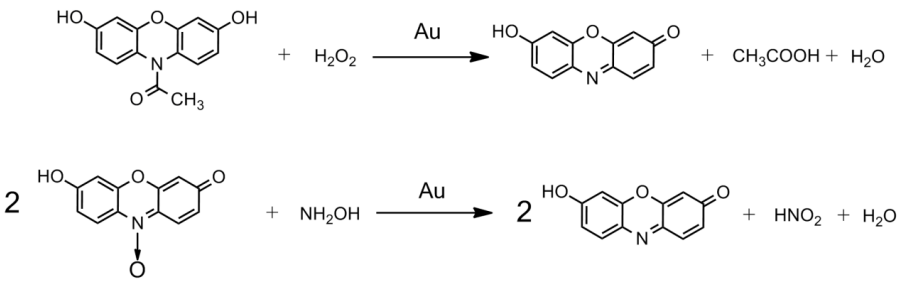

We used all neutral species in the above equations, rather than ions, as approximations. The standard formation enthalpies of the following species are taken from the CRC Handbook of Chemistry and Physics: NH_2OH (s), −114.2 kJ mol^{-1}; HNO_2 (*l*), −174.1 kJ mol^{-1}; H_2O_2 (*l*), −187.8 kJ mol^{-1}; CH_3COOH (*l*), −484.3 kJ mol^{-1}; H_2O (*l*), −285.8 kJ mol^{-1}.

The standard formation enthalpies for resazurin, resorufin, and amplex red are not available. Using the standard formation enthalpies of the gaseous atoms of C (716.7 kJ mol^{-1}), N (472.7 kJ mol^{-1}), O (249.2 kJ mol^{-1}), and H (218.0 kJ mol^{-1}), and the mean bond dissociation energies for C=C (612 kJ mol^{-1}), C–C (348 kJ mol^{-1}), C–H (412 kJ mol^{-1}), C–O (360 kJ mol^{-1}), C=O (743 kJ mol^{-1}), N–O (157 kJ mol^{-1}), N–C (305 kJ mol^{-1}), N=C (613 kJ mol^{-1}), and O–H (463 kJ mol^{-1}) bonds[52], we estimated the standard formation enthalpies to be: resazurin, 448.9 kJ mol^{-1}; resorufin, 174.7 kJ mol^{-1}; amplex red, 61.3 kJ mol^{-1}; all corresponding to their gaseous states. Using these known and estimated standard formation enthalpies, the estimated standard reaction enthalpies are $\Delta_r H°$ = −471.6 kJ mol^{-1} and −399.8 kJ mol^{-1}, for the deacetylation reaction of amplex red and the deoxygenation reaction of resazurin, respectively.

15.2 Surface restructuring dynamics should not be the mechanism

Nanoparticles, once their size is small enough, can have dynamic surface restructuring[53-55]. For colloidal Au and Pt nanoparticles of about 4−14 nm in diameter, the timescale of this dynamic restructuring is about tens to hundreds of seconds, with larger nanoparticles having slower restructuring[14,17,56]. This restructuring can be cooperative across a nanoparticle's surface[53-55,57], which could result in some correlation between reactions occurring at different locations on the same nanoparticle. Nevertheless, this restructuring is likely not the reason for the intraparticle catalytic communications observed here for the Pd and Au nanocatalysts, which are much larger and whose surfaces are further stabilized by the mesoporous silica shell. The restructuring timescale for these nanorods and nanoplates would be much longer than hundreds of seconds, thus too different from the temporal memory (10^1 to 10^2 seconds) of their intraparticle catalytic communications. Moreover, this structural dynamics should not have a directional dependence on an external electric field and would not behave like being mediated by positively-charged species.

In Section 16.3 below, we present additional evidences that the Au surface structure of Au nanorods are likely stable over the timescale of hours, further supporting that surface restructuring dynamics should not be the mechanism.

15.3 Surface plasmon resonance of Au should not be the mechanism

The $mSiO_2$-coated Au_2 nanorods and nanoplates we studied here are both plasmonic particles, and their localized surface plasmon resonances (LSPR)[9,43-49] overlap with the wavelength of the laser (532 nm) that we used to induce the fluorescence of the catalytic product resorufin. In Section 12 earlier, we showed that the intraparticle catalytic communication distances and temporal memories of Au nanorods are essentially independent of laser power density in both catalytic reactions (Supplementary Figure 24b-c and g-h). This independence supports that laser light, as well as LSPR, plays no significant roles in the observed catalytic communications.

16. Further discussions on the hole migration mechanism for intraparticle catalytic communications

16.1 Effective diffusion coefficient of hole migration for intraparticle catalytic communication

Our electric field dependence experiments showed that the intraparticle catalytic communications in Pd- and Au-based nanocatalysts all involve a movable positively-charged species, which we propose to be a surface localized hole (i.e., positive charge) that is generated during catalysis and that can hop diffusively on the surface of the nanocatalysts to affect reactions nearby, leading to intraparticle catalytic communication. The "localized" nature of this hole here could come from interactions with the $mSiO_2$ shell and that the Pd or Au surface might contain Pd_xO_y or Au_xO_y (i.e., not purely metallic palladium or gold) due to redox reactions in an aerobic environment. This type of hole migration can be over a long distance, depending on the conductivity of the materials and the presence of charge traps[58-60], and such charges can be long-lived[61], consistent with the long communication distance and temporal memory of our observed intraparticle catalytic communication. This hole migration mechanism is also related to the model proposed by Tachikawa et al. in accounting for the remote photoluminescence behavior on single semiconductor TiO_2 nanowires[62].

Using the intraparticle catalytic communication distances and temporal memories observed experimentally, we can compute the effective diffusion coefficients D_1 and D_2 for 1-D and 2-D diffusions, respectively, for the hole migration along the length of Pd and Au nanorods and across the top facet of Au nanoplates:

$$D_1 = \left\langle x^2 \right\rangle / 2t \tag{12}$$

$$D_2 = \left\langle x^2 \right\rangle / 4t \tag{13}$$

Here the communication distance x_0^{intra} is used for x, and communication temporal memory t_0^{intra} is used for t. The calculated D_1 and D_2 are *all* about 1×10^{-15} $m^2\,s^{-1}$ (Supplementary Table 2). The similarity of the effective diffusion coefficients among two different metals, three different nanocatalysts, and three distinct reactions supports that they share a common mechanism for the intraparticle catalytic communications. These effective diffusion coefficients here are small compared with those for carrier migration in semiconductor nanostructures (10^{-10} to 10^{-7} $m^2\,s^{-1}$)[63,64]. Therefore, these holes are dominantly localized, trapped charges with low mobility.

Supplementary Table 2. Parameters for the observed intraparticle and interparticle catalytic communications [a]

		Pd nanorods	Au nanorods		Au nanoplates
		Rz disproportion.	AR deacetyl.	Rz deoxygen.	Rz deoxygen.
Intra-particle	x_0^{intra} (nm)	225 ± 20 (242 ± 56) [b]	516 ± 160 (531 ± 175)	624 ± 180 (657 ± 139)	130 ± 22
	t_0^{intra} (s)	27.5 ± 2.4 (29.8 ± 9.4)	128 ± 32 (136 ± 41)	168 ± 36 (165 ± 32)	5.5 ± 0.7
	D_{eff} ($\times 10^{-15}$ m^2 s^{-1})	0.92 ± 0.08 (0.87 ± 0.22)	1.1 ± 0.4 (1.04 ± 0.37)	1.2 ± 0.4 (1.31 ± 0.29)	0.77 ± 0.17
	Amplitude	0.056 ± 0.002, 0.043 ± 0.002 [c] (0.041 ± 0.003)	0.049 ± 0.007, 0.053 ± 0.008 (0.062 ± 0.010)	0.213 ± 0.045, 0.183 ± 0.068 (0.237 ± 0.094)	0.078 ± 0.006, 0.081 ± 0.007
	Charge of messenger	positive	positive	positive	n/d
Inter-particle	x_0^{inter} (μm)	n/a	10.5 ± 3.3	9.3 ± 2.4	11.5 ± 0.7
	t_0^{inter} (s)	n/a	18.1 ± 3.8	7.7 ± 1.4	6.2 ± 0.6
	Amplitude	n/a	0.042 ± 0.003	0.037 ± 0.002	0.18 ± 0.06
	Charge of messenger	n/a	negative (CH_3COO^-)	negative (NO_2^-)	n/d
	$K_{1/2}$ of x_0^{inter} quenching by anion (μM)	n/a	0.99 ± 0.14	0.53 ± 0.12	n/d
	$K_{1/2}$ of activity promotion by anion (μM)	n/a	0.95 ± 0.15	0.46 ± 0.14	n/d
	Residual correlation	0.034 ± 0.006, 0.031 ± 0.007 [c]	0.032 ± 0.005, 0.034 ± 0.009	0.030 ± 0.004, 0.030 ± 0.008	0.081 ± 0.008, 0.080 ± 0.009

[a] Results are overall averages taking into account of all experiments, including solution flow manipulations, voltage manipulations, reactant concentration variations, and various batches of nanocatalyst samples. [b] Values in parentheses are from 2-D analysis of ρ_{τ_i,τ_j} as a function of both Δx_{ij} and $\overline{\Delta t_{ij}}$ as in Section 17. [c] Two sets of values here are from the exponential fits of one dimensional analysis of ρ_{τ_i,τ_j} vs. Δx and vs. $\overline{\Delta t_{ij}}$, respectively, as in Figure 2a and b (red).

16.2 The positively-charged species should not be conduction band charges

The positively-charged species that mediate intraparticle catalytic communication have low mobility, as shown above, and thus should be dominantly localized, trapped hole. Therefore, these holes cannot be conduction band charges of the metal nanocatalyst, which would travel fast within the nanocatalyst and thus would not decay significantly over intraparticle distance separations.

16.3 Hole migration likely occurs via hole hopping, rather than atom migration

The migration of the proposed surface localized hole should occur through hole hopping, but another possibility is through atom migration. The latter would involve a positively-charged surface atom (e.g., $Pd^{\delta+}$ or $Au^{\delta+}$) moving around on the surface, and it would need to move hundreds of nanometers (i.e., the intraparticle catalytic communication distance) over a period of 10^1 to 10^2 seconds (i.e., the intraparticle catalytic communication temporal memory). Here we provide evidence against this atom migration possibility.

In our previous study of Au nanorods in catalyzing the AR deacetylation[2], we showed that along the length of individual Au nanorods there exists an activity gradient: the center of the nanorod has the highest activity, which decays linearly toward the two ends, giving rise to a volcano activity profile along the length (Supplementary Figure 29). This activity gradient is attributable to an underlying surface defect density gradient, which is formed during the seeded crystal growth of these 1-dimensional nanocrystals[2]. Here we further examined the time dependence of

this activity gradient over the course of catalytic reactions. Supplementary Figure 29 shows that the activity gradient along the length of individual Au nanorods persists over a period of 3 hours, indicating that the underlying surface defect density gradient is stable. Therefore, the mobility of the surface Au atoms is insignificant over the timescale of hours, much longer than the observed temporal memory of intraparticle catalytic communications. This stability is also consistent with our discussions on the timescale of surface restructuring in Section 15.2, which should be very slow in these $mSiO_2$-coated Au nanorods. Atom migration is thus likely not the physical process for the proposed charge migration.

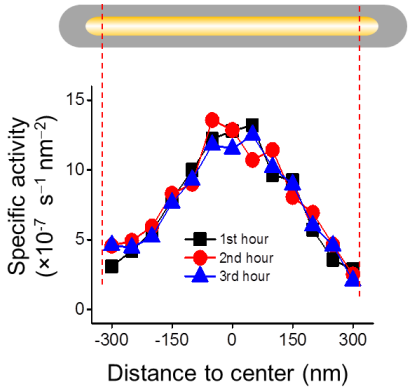

Supplementary Figure 29. Specific activity along the length of individual $mSiO_2$-coated Au nanorods in catalyzing AR deacetylation during the 1st, 2nd, and 3rd hour of catalysis. The two ends of the nanorod are excluded in the analysis. Data are averaged over ~20 nanorods, all >400 nm in length to show the general trends. The specific activity shows linear gradients from the center toward the two ends, attributable to the underlying gradient of surface defect densities along the length, as we previously showed[2].

16.4 Proton is likely not the intra-particle catalytic messenger

Proton is positively charged and exists in aqueous solution. But proton is likely not the intra-particle catalytic messenger for the following reasons:

(1) Both the disproportionation reaction and the deacetylation reaction do not produce proton as a reaction product (Figure 1b, upper and middle), but the intra-particle catalytic communication involving a positively-charged species occur in these two catalytic reactions.

(2) The deoxygenation reaction may produce proton (Figure 1b, lower), but all reactions were done in buffered slightly basic solutions.

(3) If proton diffusion were to be the intraparticle communication mechanism on the surface of Pd-/Au-nanocatalysts within the $mSiO_2$ shell, proton, owing to its small size and mediation of H-bonds in water, should be able to diffuse out of the $mSiO_2$ shell and cause inter-particle communications, which, however, in mediated by a negatively-charged product species.

(4) Proton mobility μ_q in water at room temperature is ~3.62×10^{-3} cm^2 V^{-1} s^{-1},[65] corresponding to a diffusion coefficient D of 9.29×10^{-9} m^2 s^{-1}. Proton diffusion coefficient on a membrane was measured to vary between 1.5×10^{-8} m^2 s^{-1} and 2×10^{-7} m^2 s^{-1}.[66,67] And proton diffusion coefficient in silica hydrogel is ~2×10^{-8} m^2 s^{-1}.[68] All these are orders of magnitude larger than the effective diffusion coefficient of the intraparticle catalytic messenger at ~1×10^{-15} m^2 s^{-1} (Supplementary Table 2).

16.5 Possible reasons for the non-operation of the molecular diffusion mechanism involving negatively-charged products for intra-particle catalytic communication

It is interesting to note that the molecular diffusion mechanism of negatively-charged products for the interparticle catalytic communications in Au-based nanocatalysts is not operative for intra-particle communication, even though one would normally expect that these products (i.e., acetate and nitrite), if they could diffuse between

particles, should be able to diffuse within the particles. We conjecture that this is perhaps because the mesopores of the $mSiO_2$ shell are aligned radially (they were formed by base etching from outside), as suggested in the literature[69]. This conjecture is also supported by tracking the motion of the fluorescent product resorufin, which does not diffuse laterally on the nanocatalysts before desorbing and disappearing into the solution (Supplementary Figure 5b).

16.6 Strength of catalytic communication

Regardless whether the underlying mechanism is due to a migrating hole (as for intraparticle cases) or a diffusing molecule (as for interparticle cases), these observed catalytic communications are not strong, as reflected by the small amplitudes of the decay profiles of ρ_{τ_i,τ_j}, which are mostly around 0.04 to 0.08 (Supplementary Table 2). However, there are examples of larger, more significant correlations:

a) The Au-nanorod catalyzed resazurin reduction reaction: its intra-particle catalytic communication has a correlation amplitude of 0.213 ± 0.045 (Supplementary Figure 15a-b and Supplementary Table 2).
b) The Au-nanoplate catalyzed resazurin reduction reaction: its inter-particle catalytic communication has a correlation amplitude of 0.18 ± 0.06 (Supplementary Figure 17d-e and Supplementary Table 2).

The strength of this communication, i.e., amplitude of correlation, is expected to be dependent on a number of factors. For one, the catalytic messenger generated from one site has many possible places to migrate to. For another, the strength would depend on the promotion effect by the catalytic messenger on the reaction kinetics, and for the interparticle cases, the kinetic promotion even at saturation is merely ~15% (Figure 5g and Supplementary Figure 26a and c). The amplitudes of correlation in our analysis are also expected to be smaller than the overall strength of the catalytic communications because our computed cross correlation coefficient is for temporally subsequent reactions between any "two" segments, whereas the catalytic messenger, either the proposed surface localized hole or a product anion, could migrate from one segment to *any other* segment on the same particle or to *any other* particle, for the intra- and inter-particle communications, respectively. If the correlation is summed over all possible segments, its numerical value would be significantly larger. For example, for the intra-particle catalytic communication of Pd-nanorod-catalyzed disproportionation reaction in Figure 2a (red curve), the summation over all intra-particle distance separation would give an overall correlation of ~0.18 (excluding the residual correlation values) .

17. 2-D analysis of ρ_{τ_i,τ_j} as a function of both Δx_{ij} and $\overline{\Delta t_{ij}}$ using a diffusive model for intraparticle catalytic communication

17.1 Formulation of 2-D diffusion model analysis

Assuming the motion of the catalytic messenger follows a diffusive model, we can formulate quantitatively the correlation coefficient ρ_{τ_i,τ_j} as a function of both distance separation Δx_{ij} and time delay $\overline{\Delta t_{IJ}}$, utilizing the probability density function $P_t(x)$ of displacement length *x* for a specified diffusion time *t* and the probability density function $Q_x(t)$ of diffusion time *t* for a specified displacement length *x*.

In one-dimensional Brownian motion, the probability density function $P_t(x)$ of displacement length *x* (a scalar) for a specified diffusion time *t* is:

$$P_t(x) = \frac{1}{\sqrt{\pi D t}} \exp\left(-\frac{x^2}{4Dt}\right) \qquad (14)$$

where *D* is the 1-dimensional diffusion constant. Experimentally, we observed that the correlation coefficient ρ_{τ_i,τ_j} (or ρ, to be simpler in writing) follows an exponential decay behavior with increasing time delay $\overline{\Delta t_{IJ}}$ (or *t*, to be simpler in writing) between temporally subsequent reactions:

$$\rho(t;x) = A \cdot \exp\left(-\frac{t}{t_0}\right) + c \tag{15}$$

Here x could be any value from 0 to ∞ at any given time t; t_0 is the memory time of the catalytic communication; A the correlation amplitude, and c is a residual spurious correlation. If x is constrained to a certain distance away, i.e., $x \in (x_1, x_2)$, the probability of the catalytic messenger to reach that distance range needs to be considered and this probability is $\int_{x_1}^{x_2} P_t(x)\mathrm{d}x$. Under this constraint, the correlation coefficient needs to be modified as:

$$\rho(t; x \in (x_1, x_2)) = A\exp\left(-\frac{t}{t_0}\right)\int_{x_1}^{x_2} P_t(x)\mathrm{d}x + c = A\exp\left(-\frac{t}{t_0}\right)\left[\mathrm{Erf}\left(\frac{x_2}{\sqrt{4Dt}}\right) - \mathrm{Erf}\left(\frac{x_1}{\sqrt{4Dt}}\right)\right] + c \tag{16}$$

When $x_1 = 0$ and $x_2 = \infty$, i.e., without constraining x, the above equation returns to Supplementary Equation (15) above. Supplementary Equation (16) is used to fit data such as Figure 2b in the main text.

For one-dimensional Brownian motion, the probability density function $Q_x(t)$ of diffusion time t for a specified displacement length x needs to be derived. From the probability density function $P_t(x)$, we can first deduce the probability $F(l,t)$ of displacement length in the range from 0 to l at time t:

$$F(l,t) = \int_0^l P_t(x)\mathrm{d}x = \int_0^l \frac{1}{\sqrt{\pi Dt}}\exp\left(-\frac{x^2}{4Dt}\right)\mathrm{d}x = \mathrm{Erf}\left(\frac{l}{\sqrt{4Dt}}\right) \tag{17}$$

$F(l,t)$ is essentially the survival probability that the diffusing molecule is still within a distance l from the origin at time t. Let $Q_l(t)$ be the probability density function of diffusion time t to reach a certain distance (i.e., displacement length) l, $Q_l(t)\Delta t$ is then the probability for the diffusing molecule to be at the distance l away between t and $t + \Delta t$, which is equal to $F(l,t) - F(l,t+\Delta t)$, the difference in survival probability between t and $t + \Delta t$ at the distance l. Therefore,

$$Q_l(t) \cdot \Delta t = F(l,t) - F(l,t+\Delta t) \tag{18}$$

And thus,

$$Q_l(t) = -\frac{\partial}{\partial t}F(l,t) = -\frac{\partial}{\partial t}\mathrm{Erf}\left(\frac{l}{\sqrt{4Dt}}\right) = \frac{l}{\sqrt{4\pi Dt^3}}\exp\left(-\frac{l^2}{4Dt}\right) \tag{19}$$

Replacing the variable l by x, we have:

$$Q_x(t) = \frac{x}{\sqrt{4\pi Dt^3}}\exp\left(-\frac{x^2}{4Dt}\right) \tag{20}$$

Experimentally, we observed that the correlation coefficient ρ_{τ_i,τ_j} (or ρ, to be simpler in writing) follows an exponential decay behavior with increasing distance separation Δx (or x, to be simpler in writing) where the temporally subsequent reactions occur:

$$\rho(x;t) = A \cdot \exp\left(-\frac{x}{x_0}\right) + c \tag{21}$$

Here *t* could be any value from 0 to ∞ at any given distance separation *x*; x_0 is the communication distance of the catalytic communication; *A* the correlation amplitude, and *c* is a residual spurious correlation. If *t* is constrained to a certain time range, i.e., $t \in (t_1, t_2)$, the probability of the catalytic messenger to spend this specific range of time diffusing needs to be considered and this probability is $\int_{t_1}^{t_2} Q_x(t)\mathrm{d}t$. Under this constraint, the correlation coefficient needs to be modified as:

$$\rho(x; t \in (t_1, t_2)) = A \cdot \exp(-\frac{x}{x_0}) \cdot \int_{t_1}^{t_2} Q_x(t)\mathrm{d}t + c = A \cdot \exp(-\frac{x}{x_0}) \cdot [\mathrm{Erf}(\frac{x}{\sqrt{4Dt_1}}) - \mathrm{Erf}(\frac{x}{\sqrt{4Dt_2}})] + c \quad (22)$$

When $t_1 = 0$ and $t_2 = \infty$, i.e., without constraining *t*, the above equation returns to Supplementary Equation (21) above. Supplementary Equation (22) is used to fit data as in Figure 2a in the main text.

17.2 Delayed maxima are not expected to be observable for inter-particle catalytic communications.

Both Supplementary Equations (16) and (22) predict a delayed maxima as a function of *x* or *t*, as we observed for the intraparticle catalytic communications (e.g., Figure 2a, b; green lines). These behaviors are not observed, and **are not expected to be observed, for the *inter*particle catalytic communications** because the messenger product molecules spend most of their diffusion times in the $mSiO_2$ shell, but most of their diffusion distances are in the solution; Supplementary Note 10.5).

18. Additional references

1 Huang, X. & Zheng, N. One-pot, high-yield synthesis of 5-fold twinned pd nanowires and nanorods. *J. Am. Chem. Soc.* **131**, 4602–4603 (2009).

2 Zhou, X. *et al.* Quantitative super-resolution imaging uncovers reactivity patterns on single nanocatalysts. *Nat. Nanotechnol.* **7**, 237–241 (2012).

3 Kundu, S. & Ravishankar, N. Rapid synthesis of hybrids and hollow pdo nanostructures by controlled in situ dissolution of a zno nanorod template: Insights into the formation mechanism and thermal stability. *Nanoscale* **8**, 1462-1469 (2016).

4 Jana, N. R., Gearheart, L. & Murphy, C. J. Wet chemical synthesis of high aspect ratio cylindrical gold nanorods. *J. Phys. Chem. B* **105**, 4065-4067 (2001).

5 Wang, Z. L., Mohamed, M. B., Link, S. & El-Sayed, M. A. Crystallographic facets and shapes of gold nanorods of different aspect ratios. *Surf. Sci.* **440**, L809-L814 (1999).

6 Johnson, C. J. *et al.* Growth and form of gold nanorods prepared by seed-mediated, surfactant-directed synthesis. *J. Mater. Chem.* **12**, 1765-1770 (2002).

7 Carbó-Argibay, E. *et al.* The crystalline structure of gold nanorods revisited: Evidence for higher-index lateral facets. *Angewandte Chemie (International ed. in English) FIELD Publication Date:2004* **49**, 9397-9400 (2010).

8 Katz-Boon, H. *et al.* Three-dimensional morphology and crystallography of gold nanorods. *Nano Lett.* **11**, 273–278 (2011).

9 Pérez-Juste, J., Pastoriza-Santos, I., Liz-Marzán, L. M. & Mulvaney, P. Gold nanorods: Synthesis, characterization and applications. *Coord. Chem. Rev.* **249**, 1870-1901 (2005).

10 Gai, P. L. & Harmer, M. A. Surface atomic defect structures and growth of gold nanorods. *Nano Lett.* **2**, 771-774 (2002).

11 Andoy, N. M. *et al.* Single-molecule catalysis mapping quantifies site-specific activity and uncovers radial activity gradient on single 2d nanocrystals. *J. Am. Chem. Soc.* **135**, 1845–1852 (2013).

12 Shankar, S. S. *et al.* Biological synthesis of triangular gold nanoprisms. *Nature Mater.* **3**, 482-488 (2004).

13 Botella, P., Corma, A. & Navarro, M. T. Single gold nanoparticles encapsulated in monodispersed regular spheres of mesostructured silica produced by pseudomorphic transformation. *Chemistry of Materials* **19**, 1979-1983 (2007).

14 Xu, W., Kong, J. S., Yeh, Y.-T. E. & Chen, P. Single-molecule nanocatalysis reveals heterogeneous reaction pathways and catalytic dynamics. *Nat. Mater.* **7**, 992-996 (2008).
15 Bueno, C. *et al.* The excited-state interaction of resazurin and resorufin with amines in aqueous solutions. Photophysics and photochemical reactions. *Photochem Photobiol* **76**, 385-390 (2002).
16 Balcerzyk, A. & Baldacchino, G. Implementation of laser induced fluorescence in a pulse radiolysis experiment--a new way to analyze resazurin-like reduction mechanisms. *Analyst* **139**, 1707-1712 (2014).
17 Han, K. S., Liu, G., Zhou, X., Medina, R. E. & Chen, P. How does a single pt nanocatalyst behave in two different reactions? A single-molecule study. *Nano Lett.* **12**, 1253-1259 (2012).
18 Miranda, K. M., Espey, M. G. & Wink, D. A. A rapid, simple spectrophotometric method for simultaneous detection of nitrate and nitrite. *Nitric Oxide* **5**, 62-71 (2001).
19 Beckwith, R., Cooper, J. & Margerum, D. Kinetics and mechanism of the oxidation of hydroxylamine by aqueous bromine. *Inorganic Chemistry* **33**, 5144-5150 (1994).
20 Tachikawa, T., Yonezawa, T. & Majima, T. Super-resolution mapping of reactive sites on titania-based nanoparticles with water-soluble fluorogenic probes. *ACS Nano* **7**, 263–275 (2012).
21 Roeffaers, M. B. J. *et al.* Super-resolution reactivity mapping of nanostructured catalyst particles. *Angewandte Chemie (International ed. in English) FIELD Publication Date:2004* **48**, 9285-9289 (2009).
22 Zhang, Y. *et al.* Superresolution fluorescence mapping of single-nanoparticle catalysts reveals spatiotemporal variations in surface reactivity. *Proceedings of the National Academy of Sciences* **112**, 8959–8964 (2015).
23 Decan, M. R., Impellizzeri, S., Marin, M. L. & Scaiano, J. C. Copper nanoparticle heterogeneous catalytic 'click' cycloaddition confirmed by single-molecule spectroscopy. *Nat Commun* **5**, 4612 (2014).
24 Renault, C. *et al.* Observation of nanometer-sized electro-active defects in insulating layers by fluorescence microscopy and electrochemistry. *Anal Chem* **87**, 5730-5737 (2015).
25 Skaug, M. J., Mabry, J. & Schwartz, D. K. Intermittent molecular hopping at the solid-liquid interface. *Phys Rev Lett* **110**, 256101 (2013).
26 Cordes, T. & Blum, S. A. Opportunities and challenges in single-molecule and single-particle fluorescence microscopy for mechanistic studies of chemical reactions. *Nat Chem* **5**, 993-999 (2013).
27 Ha, J. W. *et al.* Super-resolution mapping of photogenerated electron and hole separation in single metal-semiconductor nanocatalysts. *J Am Chem Soc* **136**, 1398–1408 (2014).
28 Lu, H. P., Xun, L. & Xie, X. S. Single-molecule enzymatic dynamics. *Science* **282**, 1877-1882 (1998).
29 Betzig, E. *et al.* Imaging intracellular fluorescent proteins at nanometer resolution. *Science* **313**, 1642-1645 (2006).
30 Rust, M. J., Bates, M. & Zhuang, X. Sub-diffraction-limit imaging by stochastic optical reconstruction microscopy (storm). *Nature Meth.* **3**, 793-796 (2006).
31 Hess, S. T., Girirajan, T. P. K. & Mason, M. D. Ultra-high resolution imaging by fluorescence photoactivation localization microscopy. *Biophys. J.* **91**, 4258-4272 (2006).
32 Bates, M., Huang, B., Dempsey, G. T. & Zhuang, X. Multicolor super-resolution imaging with photo-switchable fluorescent probes. *Science* **317**, 1749-1753 (2007).
33 Shroff, H., Galbraith, C. G., Galbraith, J. A. & Betzig, E. Live-cell photoactivated localization microscopy of nanoscale adhesion dynamics. *Nature Methods* **5**, 417-423 (2008).
34 Lin, H. *et al.* Mapping of surface-enhanced fluorescence on metal nanoparticles using super-resolution photoactivation localization microscopy. *ChemPhysChem* **13**, 973-981 (2012).
35 Blythe, K. L., Titus, E. J. & Willets, K. A. Comparing the accuracy of reconstructed image size in super-resolution imaging of fluorophore-labeled gold nanorods using different fit models. *Journal of Physical Chemistry C* **119**, 19333-19343 (2015).
36 Wertz, E., Isaacoff, B. P., Flynn, J. D. & Biteen, J. S. Single-molecule super-resolution microscopy reveals how light couples to a plasmonic nanoantenna on the nanometer scale. *Nano Letters* **15**, 2662-2670 (2015).
37 Zhou, X., Choudhary, E., Andoy, N. M., Zou, N. & Chen, P. Scalable parallel screening of catalyst activity at the single-particle level and sub-diffraction resolution. *ACS Catal.* **3**, 1448-1453 (2013).
38 Thompson, R. E., Larson, D. R. & Webb, W. W. Precise nanometer localization analysis for individual fluorescent probes. *Biophys. J.* **82**, 2775-2783 (2002).

39 Yildiz, A. *et al.* Myosin v walks hand-over-hand: Single fluorophore imaging with 1.5-nm localization. *Science* **300**, 2061-2065 (2003).
40 Xu, W. *et al.* Single-molecule electrocatalysis by single-walled carbon nanotubes. *Nano Lett.* **9**, 3968–3973 (2009).
41 Lide, D. R. (CRC Press, Inc., Boca Raton, 1995).
42 Zhou, X. *et al.* Quantitative super-resolution imaging uncovers reactivity patterns on single nanocatalysts. *Nat Nano* **7**, 237-241 (2012).
43 Murphy, C. J. *et al.* Gold nanorod crystal growth: From seed-mediated synthesis to nanoscale sculpting. *Curr. Opin. Coll. Interf. Sci.* **16**, 128-134 (2011).
44 Thomas, K. G., Barazzouk, S., Ipe, B. I., Joseph, S. T. S. & Kamat, P. V. Uniaxial plasmon coupling through longitudinal self-assembly of gold nanorods. *J. Phys. Chem. B* **108** (2004).
45 Shao, Y., Jin, Y. & Dong, S. Synthesis of gold nanoplates by aspartate reduction of gold chloride. *Chem. Comm.*, 1104–1105 (2004).
46 Tsuji, M., Hashimoto, M., Nishizawa, Y. & Tsuji, T. Preparation of gold nanoplates by a microwave-polyol method. *Chem. Lett.* **32**, 1114-1115 (2003).
47 Ah, C. S. *et al.* Size-controlled synthesis of machinable single crystalline gold nanoplates. *Chem. Mater.* **17**, 5558-5561 (2005).
48 Chu, H.-C., Kuo, C.-H. & Huang, M. H. Thermal aqueous solution approach for the synthesis of triangular and hexagonal gold nanoplates with three different size ranges. *Inorg. Chem.* **45**, 808-813 (2006).
49 Liu, B., Xie, J., Lee, J. Y., Ting, Y. P. & Chen, J. P. Optimization of high-yield biological synthesis of single-crystalline gold nanoplates. *J. Phys. Chem. B* **109**, 15256-15263 (2005).
50 Xu, W., Kong, J. S., Yeh, Y.-T. E. & Chen, P. Single-molecule nanocatalysis reveals heterogeneous reaction pathways and catalytic dynamics. *Nat Mater* **7**, 992-996 (2008).
51 Firoozabadi, A., Ghorayeb, K. & Shukla, K. Theoretical model of thermal diffusion factors in multicomponent mixtures. *AIChE Journal* **46**, 892-900 (2000).
52 Atkins, P. & de Paula, J. *Atkins' physical chemistry*. 8th edn, (W. H. Freeman and Company, 2006).
53 King, D. A. & Woodruff, D. P. *Phase transitions and adsorbate restructuring at metal surfaces*. (Elsevier Science, 1994).
54 Tao, F. *et al.* Reaction-driven restructuring of rh-pd and pt-pd core-shell nanoparticles. *Science* **322**, 932-934 (2008).
55 Newton, M. A. Dynamic adsorbate/reaction induced structural change of supported metal nanoparticles: Heterogeneous catalysis and beyond. *Chem. Soc. Rev.* **37**, 2644-2657 (2008).
56 Zhou, X., Xu, W., Liu, G., Panda, D. & Chen, P. Size dependent catalytic activity and dynamics of gold nanoparticles at the single-molecule level. *J. Am. Chem. Soc.* **132**, 138-146 (2010).
57 Ochoa-Daza, M. A., Zhou, X., Chen, P. & Loring, R. F. Interpreting single turnover catalysis measurements with constrained mean dwell times. *J. Chem. Phys.* **135**, 174509 (2011).
58 Chernyak, L., Osinsky, A., Fuflyigin, V. & Schubert, E. F. Electron beam-induced increase of electron diffusion length in p-type gan and algan/gan superlattices. *Appl. Phys. Lett.* **77**, 875-877 (2000).
59 Gonzalez-Vazquez, J. P., Anta, J. A. & Bisquert, J. Determination of the electron diffusion length in dye-sensitized solar cells by random walk simulation: Compensation effects and voltage dependence. *J. Phys. Chem. C* **114** 8552-8558 (2010).
60 Bian, Z., Tachikawa, T., Kim, W., Choi, W. & Majima, T. Superior electron transport and photocatalytic abilities of metal-nanoparticle-loaded tio2 superstructures. *J. Phys. Chem. C* **116**, 25444–25453 (2012).
61 Jennings, J. R. & Peter, L. M. A reappraisal of the electron diffusion length in solid-state dye-sensitized solar cells. *J. Phys. Chem. C* **111**, 16100-16104 (2007).
62 Tachikawa, T. & Majima, T. Exploring the spatial distribution and transport behavior of charge carriers in a single titania nanowire. *J. Am. Chem. Soc.* **131**, 8485–8495 (2009).
63 He, C., Zhao, L., Zheng, Z. & Lu, F. Determination of electron diffusion coefficient and lifetime in dye-sensitized solar cells by electrochemical impedance spectroscopy at high fermi level conditions. *J. Phys. Chem. C* **112**, 18730-18733 (2008).

64 van de Lagemaat, J., Zhu, K., Benkstein, K. D. & Frank, A. J. Temporal evolution of the electron diffusion coefficient in electrolyte-filled mesoporous nanocrystalline tio_2 films. *Inorg. Chim. Acta* **361**, 620-626 (2008).
65 Agmon, N. *et al.* Protons and hydroxide ions in aqueous systems. *Chem Rev* **116**, 7642-7672 (2016).
66 Gabriel, B., Prats, M. & Teissie, J. Lateral proton conduction in mixed monolayers of phosphatidylethanolamine and cetyltrimethylammonium bromide. *Biochemistry* **30**, 9359-9364 (1991).
67 Teissie, J., Prats, M., Soucaille, P. & Tocanne, J. F. Evidence for conduction of protons along the interface between water and a polar lipid monolayer. *Proc Natl Acad Sci U S A* **82**, 3217-3221 (1985).
68 Baltacioğlu, H. & Balköse, D. Diffusion of protons in silica hydrogel. *Colloid and Polymer Science* **267**, 460-464 (1989).
69 Gorelikov, I. & Matsuura, N. Single-step coating of mesoporous silica on cetyltrimethyl ammonium bromide-capped nanoparticles. *Nano Lett* **8**, 369-373 (2008).